

ABSTRACT

ZILBERTER, ILYA ALEXANDROVICH. LES/RANS Simulations of High Speed Mixing Processes. (Under the direction of Dr. Jack Edwards.)

A hybrid Large Eddy Simulation / Reynolds Averaged Navier Stokes (LES/RANS) model is presented and used to simulate two high-speed mixing experiments. The solver blends a RANS method with a Menter BSL turbulence closure near the walls with an LES model with Lenormand subgrid closure in the free stream. Large scale turbulence is induced and sustained using a recycling/rescaling technique. Simulations of air, argon, and helium streams mixing with a parallel Mach 1.3 air stream are performed, as well as sonic injection of ethylene, argon, and helium into a Mach 2.0 air cross-stream. Turbulence statistics are collected for all cases and used to evaluate two eddy viscosity models for the turbulent scalar flux. A new alternative to the gradient-diffusion formulation for the scalar fluxes is also proposed and evaluated.

© Copyright 2012 by Ilya Alexandrovich Zilberter

All Rights Reserved

LES/RANS Simulations of High Speed Mixing Processes

by
Ilya Alexandrovich Zilberter

A thesis submitted to the Graduate Faculty of
North Carolina State University
in partial fulfillment of the
requirements for the Degree of
Master of Science

Aerospace Engineering

Raleigh, North Carolina

2012

APPROVED BY:

Dr. Hassan Hassan

Dr. Hong Luo

Dr. Jack Edwards
Chair of Advisory Committee

DEDICATION

To Mom and Dad. Thank you for your love and support.

BIOGRAPHY

Ilya Zilberter was born on August 13, 1987, in the town of Liepaja in the Latvian SSR. His family moved to North Carolina in 1995, eventually settling down in Apex. He attended middle school and high school at Cary Academy, graduating in 2005 and going on to pursue a degree in aeronautical engineering at the California Institute of Technology. During his senior year propulsion course, taught by Dr. Jay Polk, Ilya was introduced both to CFD and supersonic propulsion, which would continue to be two of his main areas of interest. After graduating Caltech in 2009 with a BS in aeronautics, Ilya went on to attend graduate school at North Carolina State University, where he has been working under the direction of Dr. Edwards.

Outside of work and academics, Ilya enjoys drawing, playing the guitar, skiing, and hiking.

ACKNOWLEDGEMENTS

I would foremost like to thank my advisor, both for being a bottomless source of knowledge and for his patience. I have learned a great deal about CFD from him, both during the course of this work and from his classes. I would also like to thank Dr. Hassan and Dr. Luo for serving on my committee and teaching some very illuminating courses.

Thanks also to my coworkers, who have provided me with a lot of help and some well-needed distractions when things got overwhelming.

This work has been supported by the Air Force Research Laboratory, under contract FA8650-08-D-2844, through a subcontract with Taitech, Inc. (Taitech contract TS10-44-05-001). A final thank you to Department of Defence HPC resources and NC State University's Information Technologies Division, who have provided the computing resources for this project.

TABLE OF CONTENTS

List of Tables	vi
List of Figures	vii
Nomenclature	ix
Chapter 1 Introduction	1
Chapter 2 Governing Equations	3
2.1 Gas Flow Equations	3
2.2 Reynolds-Averaged Navier-Stokes (RANS) Equations	5
2.3 Filtered Navier-Stokes Equations	7
2.4 Turbulence Modeling	8
2.4.1 Menter Baseline Model (Menter BSL)	9
2.4.2 Lenormand Subgrid Model	10
Chapter 3 Numerical Formulation	11
3.1 Flux Discretization	11
3.1.1 Low-Diffusion Flux Splitting Scheme (LDFSS)	12
3.1.2 Piecewise Parabolic Method (LD-PPM)	14
3.1.3 Ducros Switch	14
3.2 Time Intergration	15
3.3 Turbulence Recycling/Re-scaling	16
Chapter 4 LES/RANS Simulations of Planar Mixing Layer	17
4.1 Calculation Details	17
4.2 Comparison with Experiment	19
Chapter 5 Model Evaluation	25
5.1 Data Extraction	25
5.2 Model Form Evaluation	28
Chapter 6 LES/RANS Simulations of Sonic Injection	40
6.1 Calculation Details	40
6.2 Comparison With Experiment	42
6.3 Gradient Model Evaluation	43
6.4 Effect of Convergence	51
Chapter 7 Summary and Conclusions	62
References	64

LIST OF TABLES

Table 2.1	Menter BSL Model Constants	10
Table 4.1	Simulated Flow Conditions	19
Table 6.1	Simulated Flow Conditions, Lin et al. Experiment	41

LIST OF FIGURES

Figure 4.1	Schematic of computational domain (Barre, et al. experiment)	18
Figure 4.2	Snapshots from simulation of Barre, et al. mixing layer (clockwise from upper left: temperature, mass fraction, transverse velocity, pressure) . . .	20
Figure 4.3	Velocity profiles at different axial stations (Barre, et al. experiment) . . .	21
Figure 4.4	Mixing layer spreading rate (Barre, et al. experiment)	22
Figure 4.5	rms axial velocity fluctuation intensity profiles (near-field stations)	22
Figure 4.6	rms axial velocity fluctuation intensity profiles (far-field stations)	23
Figure 4.7	Resolved Reynolds shear stress versus predictions deduced by Barre, et al.	23
Figure 4.8	rms temperature fluctuation predictions (K) versus experimental data . .	24
Figure 5.1	Turbulent Schmidt number profiles (air-air mixing)	27
Figure 5.2	Turbulent Schmidt number profiles (air-argon mixing)	27
Figure 5.3	Turbulent Schmidt number profiles (air-helium mixing)	28
Figure 5.4	scalar fluctuation energy balance (air-air mixing)	29
Figure 5.5	Scalar fluctuation energy balance (air-argon mixing)	29
Figure 5.6	Scalar fluctuation energy balance (air-helium mixing)	30
Figure 5.7	Mass diffusivities predicted by different models (air-air mixing)	31
Figure 5.8	Mass diffusivities predicted by different models (air-argon mixing)	32
Figure 5.9	Mass diffusivities predicted by different models (air-helium mixing) . . .	32
Figure 5.10	Scalar production rates predicted by different 'optimized' models (air-air mixing)	33
Figure 5.11	Scalar production rates predicted by different 'optimized' models (air- argon mixing)	33
Figure 5.12	Scalar production rates predicted by different 'optimized' models (air- helium mixing)	34
Figure 5.13	Scalar dissipation rates predicted by different models extracted along line of peak dissipation rates	36
Figure 5.14	Scalar dissipation rates predicted by different models ($X = 0.25m$)	37
Figure 5.15	Modeled and actual concentration variance extracted along centerline of flow	38
Figure 5.16	Modeled and actual concentration variance ($X = 0.25m$)	39
Figure 6.1	Schematic of computational domain (Lin, et. al experiment)	41
Figure 6.2	Snapshot of density contours for ethylene injection	42
Figure 6.3	Instantaneous ethylene mass fraction predictions (top) compared with NO PLIF snapshots (bottom)	43
Figure 6.4	Comparison of ethylene mole fractions from simulation (top) and NO- PLIF data (bottom)	44
Figure 6.5	Ethylene mole fractions at $x/d = 5$. Values range from 0 to 0.7	44
Figure 6.6	Ethylene mole fractions at $x/d = 25$. Values range from 0 to 0.25	45

Figure 6.7	Scalar production rates for Ethylene, $x/d = 5$. Values range from 0 to 1600 kg/m^3s	46
Figure 6.8	Scalar production rates for Ethylene, $x/d = 25$. Values range from 0 to 50 kg/m^3s	47
Figure 6.9	Mass diffusivities for Ethylene, $x/d = 25$. Values range from 0 to 0.075 m^2/s	48
Figure 6.10	Exact versus modeled scalar fluxes for gradient-diffusion model (ethyene injection, $x/d=25$)	49
Figure 6.11	Exact versus modeled scalar fluxes for new model ethylene injection, $x/d = 25$)	51
Figure 6.12	Scalar production rates for Ethylene, $x/d = 5$. Values range from 0 to 1600 kg/m^3s	52
Figure 6.13	Scalar production rates for Ethylene, $x/d = 15$. Values range from 0 to 100 kg/m^3s	53
Figure 6.14	Scalar production rates for Ethylene, $x/d = 25$. Values range from 0 to 50 kg/m^3s	54
Figure 6.15	Scalar production rates for Argon, $x/d = 5$. Values range from 0 to 600 kg/m^3s	55
Figure 6.16	Scalar production rates for Argon, $x/d = 15$. Values range from 0 to 80 kg/m^3s	56
Figure 6.17	Scalar production rates for Argon, $x/d = 25$. Values range from 0 to 25 kg/m^3s	57
Figure 6.18	Scalar production rates for Helium, $x/d = 5$. Values range from 0 to 300 kg/m^3s	58
Figure 6.19	Scalar production rates for Helium, $x/d = 15$. Values range from 0 to 15 kg/m^3s	59
Figure 6.20	Scalar production rates for Helium, $x/d = 25$. Values range from 0 to 3 kg/m^3s	60
Figure 6.21	Scalar production rates for Argon, $x/d = 15$. Values range from 0 to 80 kg/m^3s	61

NOMENCLATURE

Roman Letters

a	sound speed
A	cell face area
$A_1 - A_5$	constant for heat capacity polynomials
$\tilde{A} - \tilde{G}$	flux Jacobians
arg_1	Menter BSL model function
$C_1 - C_4$	scalar flux model constants
C_M	LES model constant
C_P	specific heat at constant pressure
C_X	Model constant for Brinckman, et. al model
C_Y	Model constant for Xiao, et. al model
CD_{kw}	Menter BSL model function
d	injector diameter
d	wall distance function
D	laminar species diffusion
e	total energy per unit mass
E	flux vector
f	mixture fraction
F_1	blending function for Menter model
G	filter function
h	enthalpy per unit mass
k	turbulent kinetic energy
L, D, U	matrix components for ILU decomposition
M	Mach number
M_c	convective Mach number
M_n	molecular weight
n	cell outward normal vector
p	pressure
P_k	turbulent kinetic energy production rate
P_s	scalar variance production rate
Pr	Prandtl number
q	laminar heat flux
Q	generic flow quantity
\vec{Q}	flow solution vector

R	gas constant
\vec{R}	residual vector
S	vorticity vector
\vec{S}	source term vector
Sc	Schmidt number
Sc_t	turbulent Schmidt number
t	time
T	temperature
t_{ij}	stress tensor
u,v,w	velocity variables
U	flow speed or contravariant velocity
\vec{U}	conserved variable vector
V	species diffusion velocity
\vec{V}	primitive variable vector
x,y,z	position variables
X	mole fraction
Y	mass fraction

Greek Letters

ρ	density
$\nu_{t,mass}$	turbulent mass diffusivity
$\nu_{t,mom}$	turbulent momentum eddy viscosity
ϵ	turbulent kinetic energy dissipation rate
ϵ_S	scalar dissipation rate
σ	concentration variance
μ	laminar fluid viscosity
δ_{ij}	Kronecker delta
ψ_{ij}	mixing coefficient
τ_{ij}	Reynolds stress tensor
ζ	integration variable for filtered Navier-Stokes equations
Δ	cell volume
ω	turbulence frequency
μ_t	turbulent viscosity
ϕ	blending function for Menter model
σ_k	model constant for Menter model

σ_ω	model constant for Menter model
β	model constant for Menter model
γ	model constant for Menter model
β_*	model constant for Menter model
Γ	blending function
α_1	boundary layer model constant
λ_C	blending function model constant
Ω	cell volume

Superscripts

c	convective component
p	pressure componente
n	time level
k	sub-iteration level

Subscripts

i,j,k	cell indices, spatial coordinates
T	turbulent
L	laminar
max	maximum
min	minimum
mix	mixture
n	species
opt	optimal
1/2	cell interface
L,R	left and right states
RANS	RANS solution
buf	buffer region

Accents

\rightarrow	vector
$—$	time-averaged quantity
\sim	density-averaged quantity
$'$	time-fluctuation
$''$	mass-fluctuation

Abbreviations

BSL	baseline
ILU	incomplete lower/upper
LES	large eddy simulation
LD	low-dissipation
LDFSS	low-diffusion flux-splitting scheme
NS	number of species
PLIF	planar laser-induced fluorescence
PPM	piecewise parabolic method
RANS	Reynolds-averaged Navier Stokes
SPGS	symmetric planar Gauss-Seidel

Chapter 1

Introduction

A major uncertainty in Reynolds-averaged Navier-Stokes (RANS) modeling of supersonic combustion processes is the treatment of turbulence effects on scalar mixing. Typically, the scalar flux is modeled using a gradient-diffusion form,

$$\overline{\rho u_j'' Y''} = -\bar{\rho} \nu_{t, mass} \frac{\partial \tilde{Y}}{\partial x_j} \quad (1.1)$$

where $\nu_{t, mass}$ is a diffusivity associated with scalar transport. Usually, this mass diffusivity is assumed to be related to the eddy viscosity as calculated by a standard turbulence model by a constant turbulent Schmidt number. However, many studies [2] [22] have shown that RANS calculations of supersonic combustion processes are extremely sensitive to small changes in the turbulent Schmidt number. In their simulations of isolator / combustor flowfields with ethylene injection, Baurle and Eklund [2] showed that conditions ranging from flame blowoff to inlet unstart due to excessive heat release could be obtained from small variations in the turbulent Schmidt number. Similar results were obtained by Vyas, et al [22] in their calculations of hydrogen-air combustion during dual-mode operation in the University of Virginia's supersonic combustion facility. They were forced to adjust their (constant) turbulent Schmidt numbers to place the shock train at the experimentally-determined conditions. Clearly, this poses a large problem for attempting to conduct predictive studies of combustion using RANS simulations.

The present work considers two approaches to calculate the mass diffusivity as part of a RANS-level flow solution. The first approach, by Brinckman, et al. [6] extends a $k - \epsilon$ formulation for temperature fluctuations developed by Sommer, et al. [19] to calculate scalar fluctuations as well. The model uses flow data to approximate the mixture fraction dissipation rate ϵ_S and mixture fraction variance $\sigma = \overline{f'' f''}$, which are then used to calculate the mass diffusivity as

$$\nu_{t, mass} = C_X k \sqrt{\frac{k}{\epsilon} \frac{\sigma}{\epsilon_S}} \quad (1.2)$$

where k is the turbulence kinetic energy, or $1/2\overline{u_i''u_i''}$. This is obtained through standard transport equations with compressibility corrections. The mixture fraction variance and dissipation rate are both calculated from mean mixture fraction gradients. In regions where these gradients are zero, the mass diffusivity can reach anomalous values, requiring a limiter to be employed, in this case,

$$\frac{1}{S_{c_{t,min}}} \nu_{t,mom} > \nu_{t,mass} > \frac{1}{S_{c_{t,max}}} \nu_{t,mom} \quad (1.3)$$

where $\nu_{t,mom}$ is the turbulent eddy viscosity used in the momentum equations.

The second approach considered is by Xiao, et al., [24] which employs an extension of the $k - \zeta$ (k-entropy) model of Robinson and Hassan [18]. Here, the mass diffusivity is calculated from the sum of the scalar variances,

$$\sigma = \overline{\sum_k Y_k'' Y_k''} \quad (1.4)$$

and scalar dissipation rate

$$\rho \epsilon_S = \sum_k \rho D \left(\frac{\partial Y_k''}{\partial x_j} \right) \left(\frac{\partial Y_k''}{\partial x_j} \right) \quad (1.5)$$

The mass diffusivity itself is modeled as

$$\nu_{t,mass} = \frac{1}{2} \left(C_Y k \frac{\sigma}{\epsilon_S} + \frac{\nu_{t,mom}}{\sigma_h} \right) \quad (1.6)$$

Because the sum of scalar variances is not conserved in a reacting flow, an extra closure term is needed, based on the species production rates: $2 \sum_k \overline{\dot{\omega}_k Y_m''}$. In this work, only non-reactive flows are dealt with, and this term need not be considered. However, this aspect of the model may present a problem in reactive flow modeling. Additionally, as with the previous model, areas with small or zero concentration gradients may create anomalous results, so a limiter must also be applied to the mass diffusivity.

Although both of these models have shown to give better results than a constant Schmidt number assumption under certain conditions, neither has been fully evaluated, and as of yet there have been no experiments to assess the validity of the modeling of their individual terms. Thus in this work, two sets of numerical experiments are carried out using LES/RANS modeling to collect the necessary data to evaluate these models and assess their performance at conditions relevant to scramjet operation. The simulations are based on a high-speed planar mixing experiment by Barre, et al. [1] and on a sonic injection experiment by Lin, et al. [15] After initial validation of the LES/RANS model, the flow conditions are changed, and the LES/RANS results are used as a truth model to assess the above approaches to calculate scalar mixing.

Chapter 2

Governing Equations

This section details the governing equations of the gas flow, as well as the models used to calculate the effects of turbulence and compressibility on the flow. Briefly, the LES/RANS simulations solve the compressible Navier-Stokes equations for a binary mixture of ideal, non-reacting gases. The Menter BSL[17] model is used to calculate the turbulent eddy viscosity for the Reynolds-averaged Navier Stokes equations (RANS); this is blended with a subgrid model by Lenormand[14] for the LES (Large Eddy simulation) calculations.

2.1 Gas Flow Equations

The mean flow of the fluid is determined by solving the compressible Navier-Stokes equations and the energy conservation equation, extended for a binary mixture. The species continuity equation in tensor notation, is

$$\frac{\partial \rho_n}{\partial t} + \frac{\partial(\rho_n(u_j + V_{n,j}))}{\partial x_j} = 0 \quad (2.1)$$

Here, ρ_n is the species density; n ranges from 1 to 2, since we are considering two species. The instantaneous forms of the Navier Stokes equations for the full mixture are as follows:

$$\frac{\partial \rho}{\partial t} + \frac{\partial}{\partial x_i}(\rho u_i) = 0 \quad (2.2)$$

$$\frac{\partial}{\partial t}(\rho u_i) + \frac{\partial}{\partial x_j}(\rho u_i u_j) = -\frac{\partial p}{\partial x_i} + \frac{\partial t_{ij}}{\partial x_j} \quad (2.3)$$

$$\frac{\partial}{\partial t} \left[\rho \left(e + \frac{1}{2} u_i u_i \right) \right] + \frac{\partial}{\partial x_j} \left[\rho u_j \left(h + \frac{1}{2} u_i u_i \right) \right] = \frac{\partial}{\partial x_j} (u_i t_{ij}) - \frac{\partial q_j}{\partial x_j} \quad (2.4)$$

where e is the specific internal energy, $h = e + p/\rho$ is the specific enthalpy, and q_j is the heat transfer rate. The viscous stress tensor t_{ij} can be taken for an ideal gas to be

$$t_{ij} = \mu \left(\frac{\partial u_i}{\partial x_j} + \frac{\partial u_j}{\partial x_i} \right) - \frac{2}{3} \mu \frac{\partial u_k}{\partial x_k} \delta_{ij} \quad (2.5)$$

where μ is the viscosity of the fluid. As a closure for the thermodynamic state of the mixture, the ideal gas law is used:

$$P = \rho R_{mix} T \quad (2.6)$$

The mixture state variables are defined using the properties of each gas, as follows:

$$P = \sum_{n=1}^{NS} P_n \quad (2.7)$$

$$R_{mix} = R \sum_{n=1}^{NS} \frac{Y_n}{M_n} \quad (2.8)$$

$$\rho = \frac{P}{R_{mix} T} \quad (2.9)$$

$$h(T) = \sum_{n=1}^{NS} Y_n h_n(T) \quad (2.10)$$

$$e = h - \frac{P}{\rho} \quad (2.11)$$

$$Y_n = \frac{\rho_n}{\rho} \quad (2.12)$$

where NS is the number of species (two), P_n is the partial pressure of species n , R_{mix} is the mixture gas constant, R is the universal gas constant, Y_n is the species mass fraction, M_n is the species molecular weight, T is the temperature, and h_n is the specific enthalpy of species n . the specific enthalpy for each species is defined as:

$$h_n(T) = h_{f_n}^0 + \int_{T^0}^T C_{P_n}(T) dT \quad (2.13)$$

where h_f^0 and T^0 are reference quantities. The specific heat of each species, C_{P_n} is defined by polynomial curve fits taken from McBride[16]:

$$C_{P_n} = R(A_{1,n} + A_{2,n}T + A_{3,n}T^2 + A_{4,n}T^3 + A_{5,n}T^5) \quad (2.14)$$

The laminar viscosity of the mixture is determined via Wilke's law:

$$\mu = \sum_{n=1}^{NS} \left[X_n \mu_n \left(\sum_{n=1}^{NS} X_n \psi_{ij} \right)^{-1} \right] \quad (2.15)$$

where X_n is the mole fraction of species n and $\psi_{i,j}$ is the mixing coefficient, defined as:

$$\psi_{ij} = \frac{\left(1 + \sqrt{\frac{\mu_i}{\mu_j}} \left(\frac{M_j^{\frac{1}{4}}}{M_i} \right)^2 \right)}{\sqrt{8 \left(1 + \frac{M_i}{M_j} \right)}} \quad (2.16)$$

The species diffusion velocity is determined using Fick's Law:

$$V_{n,j} = -\frac{\mu}{Sc} \frac{\partial Y_n}{\partial x_j} \quad (2.17)$$

where Sc is the Schmidt number. The heat flux vector is defined as:

$$q_i = \mu \sum_{n=1}^{NS} \frac{Y_n C_{P_n}}{Pr} \frac{\partial T}{\partial x_i} \quad (2.18)$$

where Pr is the Prandtl number. In the present study, the Prandtl and Schmidt numbers were 0.72 and 0.5, respectively.

These equations may be solved to obtain a more or less 'exact' solution for the flow; however, capturing the small turbulent and eddy effects would require a prohibitively fine mesh grid. To save computing costs, we solve either the filtered Navier-Stokes equations when performing a LES simulation or the Reynolds-averaged Navier-Stokes equations, which are described in the following sections.

2.2 Reynolds-Averaged Navier-Stokes (RANS) Equations

The RANS equations provide a way to quickly calculate the mean flow variables using relatively little computational resources. Here, only the largest scales are resolved while the effects of turbulence on the flow are modeled, eliminating the need for a fine mesh resolution[23]. In order to remove fluctuations due to small-scale turbulence while maintaining mean time-dependent terms, we introduce Reynolds averaging, defined such that for any flow quantity Q , the Reynolds averaged property

$$\overline{Q} = \frac{1}{T} \int_T Q(t) dt \quad (2.19)$$

where T is some finite time. This essentially splits Q into a time-averaged quantity \overline{Q} and fluctuations in the quantity Q' ,

$$Q = \overline{Q} + Q' \quad (2.20)$$

Note that $\overline{Q'} = 0$. While this eliminates small time-dependent fluctuations, because we are dealing with a compressible system, density-based fluctuations also need to be accounted for. Therefore, we define a Favre average to be:

$$\tilde{Q} = \frac{\overline{\rho Q}}{\bar{\rho}} \quad (2.21)$$

where

$$Q = \tilde{Q} + Q'' \quad (2.22)$$

$$\overline{\rho Q''} = 0 \quad (2.23)$$

We can apply Favre averaging to the governing equations, beginning with decomposing the flow properties as follows:

$$\left. \begin{aligned} u_i &= \tilde{u}_i + u'' \\ \rho &= \bar{\rho} + \rho' \\ p &= P + p' \\ h &= \tilde{h} + h'' \\ e &= \tilde{e} + e'' \\ T &= \tilde{T} + T'' \\ q_j &= q_{L_j} + q'_j \end{aligned} \right\} \quad (2.24)$$

After performing mass-averaging operations on the conservation equations, we obtain the following relations:

$$\frac{\partial \bar{\rho}_n}{\partial t} + \frac{\partial (\bar{\rho}_n (\tilde{u}_i + \tilde{V}_{n,i}))}{\partial x_i} = 0 \quad (2.25)$$

$$\frac{\partial \bar{\rho}}{\partial t} + \frac{\partial}{\partial x_i} (\bar{\rho} \tilde{u}_i) = 0 \quad (2.26)$$

$$\frac{\partial}{\partial t} (\bar{\rho} \tilde{u}_i) + \frac{\partial}{\partial x_j} (\bar{\rho} \tilde{u}_j \tilde{u}_i) = -\frac{\partial P}{\partial x_i} + \frac{\partial}{\partial x_j} [\overline{t_{ij}} - \overline{\rho u_j'' u_i''}] \quad (2.27)$$

$$\begin{aligned} & \frac{\partial}{\partial t} \left[\bar{\rho} \left(\tilde{e} + \frac{\tilde{u}_i \tilde{u}_i}{2} \right) + \frac{\overline{\rho u_i'' u_i''}}{2} \right] + \frac{\partial}{\partial x_j} \left[\bar{\rho} \tilde{u}_j \left(\tilde{h} + \frac{\tilde{u}_i \tilde{u}_i}{2} \right) + \tilde{u}_j \frac{\overline{\rho u_i'' u_i''}}{2} \right] \\ &= \frac{\partial}{\partial x_j} \left[-q_{L_j} - \overline{\rho u_j'' h''} + \overline{t_{ij} u_i''} - \overline{\rho u_j'' \frac{1}{2} u_i'' u_j''} \right] + \frac{\partial}{\partial x_j} [\tilde{u}_i (\overline{t_{ij}} - \overline{\rho u_i'' u_j''})] \end{aligned} \quad (2.28)$$

$$P = \bar{\rho} R_{mix} \tilde{T} \quad (2.29)$$

Several terms of interest arise in this form of the equations. Foremost for this study is the Favre-averaged species diffusion, $\tilde{V}_{n,i} = V_{n,i}^t - V_{n,i}$. The new term $V_{n,i}^t$ is the turbulent species diffusion, defined as

$$\bar{\rho} V_{n,i}^t \equiv \overline{\rho u_i'' Y_n''} \quad (2.30)$$

Note that the left hand side is equivalent to the turbulent scalar flux. Because the fluctuating quantities are not directly resolved in a RANS simulation, this is modeled similarly to the laminar species diffusion,

$$\overline{\rho u_i'' Y_n''} = -\bar{\rho} \nu_{t, mass} \frac{\partial \tilde{Y}_n}{\partial x_i} \quad (2.31)$$

This study will investigate several closures for the mass diffusivity $\nu_{t, mass}$.

Another important term is the Reynolds stress tensor,

$$\bar{\rho} \tau_{ij} \equiv \overline{-\rho u_i'' u_j''} \quad (2.32)$$

This is defined using the Boussinesq approximation to be

$$\rho \tau_{ij} = \mu_T \left(\frac{\partial u_i}{\partial x_j} + \frac{\partial u_j}{\partial x_i} \right) - \frac{2}{3} \bar{\rho} k \delta_{ij} \quad (2.33)$$

where k is the turbulent kinetic energy per unit mass, defined as

$$k = \frac{1}{2} \overline{u_i'' u_i''} \quad (2.34)$$

μ_T is the turbulent eddy viscosity, which is approximated by the turbulence models of Menter and Lenormand described in the next sections. The term $\overline{\rho u_j'' h''}$ is the turbulent heat flux vector, and is modeled as follows:

$$q_{Tj} \equiv \overline{\rho u_j'' h''} = -\frac{\mu_T}{Pr_T} \frac{\partial \tilde{h}}{\partial x_j} \quad (2.35)$$

where Pr_T is the turbulent Prandtl number, usually assumed to be 0.9. The molecular diffusion term $\overline{t_{ij} u_i''}$ and the turbulent transport term $\frac{\overline{\rho u_j'' u_i'' u_i''}}{2}$ can be neglected for flows below the hypersonic range.

2.3 Filtered Navier-Stokes Equations

When performing Large Eddy Simulations, the larger scales of turbulence are resolved directly while only the smallest subgrid scales (SGS) are modeled. While this requires more computa-

tional resources, it allows us to obtain relatively detailed, time-accurate solutions for the flow. Additionally, the fluctuating terms involved in the Reynolds stresses and turbulent scalar transport can be computed exactly, providing a basis of comparison for modeled terms in the RANS simulations. LES thus requires the development and solution of the filtered Navier-Stokes equations. Given a flow property Q ,

$$Q = \bar{Q} + Q' \quad (2.36)$$

where \bar{Q} is the filtered component and Q' is the SGS component. The filtered quantity is defined (for a generic filter G) as

$$\bar{Q}_i(x_i, t) = \int \int \int G(x_i - \xi_i, \Delta) A_i(\xi, \Delta) d^3 \xi_i \quad (2.37)$$

The filter function is normalized:

$$\int \int \int G(x_i - \xi_i, \Delta) d^3 \xi_i = 1 \quad (2.38)$$

where

$$\Delta = \sqrt[3]{\Delta_x \Delta_y \Delta_z} \quad (2.39)$$

and Δ_i are the cell dimensions. The filtered forms of the Navier-Stokes equations are as follows:

$$\frac{\partial \bar{\rho}_n}{\partial t} + \frac{\partial (\bar{\rho}_n (\tilde{u}_i + \tilde{V}_{n,i}))}{\partial x_i} = 0 \quad (2.40)$$

$$\frac{\partial}{\partial t} (\bar{\rho} \tilde{u}_i) + \frac{\partial}{\partial x_j} (\bar{\rho} \tilde{u}_j \tilde{u}_i) = -\frac{\partial \bar{P}}{\partial x_i} + \frac{\partial}{\partial x_j} [\bar{t}_{ij} - \tau_{ij}] \quad (2.41)$$

$$\frac{\partial}{\partial t} (\bar{\rho} \tilde{E}) + \frac{\partial}{\partial x_j} (\bar{\rho} \tilde{H} \tilde{u}_j) = \frac{\partial}{\partial x_j} [\tilde{u}_i (\bar{t}_{ij} + \tau_{ij}) - (\bar{q}_j + q_{T,j})] \quad (2.42)$$

Closures similar to those used in the RANS equations can be applied for the turbulent shear stress, diffusion velocity, and heat fluxes.

2.4 Turbulence Modeling

The simulations in this study used two turbulence models; Menter BSL[17], which is a hybrid of Wilcox's $k - \omega$ model[23] near the wall and a $k - \epsilon$ model elsewhere, was used for the RANS simulations and near the wall in the LES/RANS simulations. In the outer flow regions in the LES/RANS simulations, a subgrid model by Lenormand[14] was utilized.

2.4.1 Menter Baseline Model (Menter BSL)

The Menter BSL Model blends the $k - \epsilon$ (where ϵ is the turbulent kinetic energy dissipation rate per unit mass) and $k - \omega$ (where ω is the specific turbulent dissipation) models by rewriting the $k - \epsilon$ equations in terms of ω . The extra term that results is then multiplied by a blending function F_1 , which forces the model to revert to a standard $k - \omega$ formulation at the wall. The turbulent eddy viscosity is defined as:

$$\mu_T = \rho \nu_{T,RANS} = \rho \frac{k}{\omega} \quad (2.43)$$

and the $k - \omega$ equations are:

$$\frac{\partial \rho k}{\partial t} + \frac{\partial \rho k u_j}{\partial x_j} = \mu_T S^2 - \rho \beta_* k \omega + \frac{\partial \left[(\mu + \mu_t) \frac{\partial k}{\partial x_j} \right]}{\partial x_j} \quad (2.44)$$

$$\frac{\partial \rho \omega}{\partial t} + \frac{\partial \rho \omega u_j}{\partial x_j} = \rho \gamma S^2 - \beta \rho \omega^2 + \frac{\partial \left[(\mu + \sigma_\omega \mu_t) \frac{\partial \omega}{\partial x_j} \right]}{\partial x_j} + 2(1 - F_1) \rho \sigma_{\omega 2} \frac{1}{\omega} \frac{\partial k}{\partial x_j} \frac{\partial \omega}{\partial x_j} \quad (2.45)$$

the magnitude of the vorticity vector S is given by:

$$S = \left[\frac{\partial u_i}{\partial x_j} \frac{\partial u_j}{\partial x_i} + \frac{\partial u_i}{\partial x_j} \frac{\partial u_i}{\partial x_j} - \frac{2}{3} \left(\frac{\partial u_i}{\partial x_i} \right)^2 \right]^{\frac{1}{2}} \quad (2.46)$$

The blending function F_1 is:

$$F_1 = \tanh(arg_1^4), \quad (2.47)$$

$$arg_1 = \min \left[\max \left(\frac{\sqrt{k}}{0.009 \omega y}, \frac{4 \rho \sigma_{\omega 2} k}{C D_{kw} y^2} \right) \right] \quad (2.48)$$

Here y is the distance to the nearest wall. $C D_{kw}$ is given as:

$$C D_{kw} = \max \left(2 \rho \sigma_{\omega 2} \frac{1}{\omega} \frac{\partial k}{\partial x_j} \frac{\partial \omega}{\partial x_j}, 10^{-20} \right) \quad (2.49)$$

The blending function is also applied to the model constants, shown in Table 2.1. :

$$\phi = F_1 \phi_1 + (1 - F_1) \phi_2 \quad (2.50)$$

where ϕ_1 indicates a $k - \omega$ constant and ϕ_2 a $k - \epsilon$ constant.

Table 2.1: Menter BSL Model Constants

Model Constant	(inner) $k - \omega$ (Wilcox)	(outer) $k - \epsilon$
σ_k	0.5	1.0
σ_ω	0.5	0.956
β	0.0750	0.0828
β_*	0.09	0.09
γ	0.5532	0.4404

2.4.2 Lenormand Subgrid Model

When performing hybrid Large Eddy Simulation(LES)/RANS studies, the larger turbulent flow structures are resolved directly throughout most of the flow, with a separate subgrid turbulence model applied to account for the effects of the smallest scales. For this, the turbulence model by Lenormand, et al. was used. Near the wall, where turbulent eddies become uniformly small, a blending function was used to switch the turbulence model back to Menter BSL. Thus, the kinematic eddy viscosity is defined as follows:

$$\nu_T = \Gamma \nu_{T,RANS} + (1 - \Gamma) \nu_{T,LES} \quad (2.51)$$

$$\nu_{T,LES} = \Gamma \kappa C_\mu^{1/4} k^{1/2} d + (1 - \Gamma) \bar{\nu}_{T,LES} \quad (2.52)$$

$$\bar{\nu}_{T,LES} = C_M S^{1/2} (q^2)^{1/4} \Delta^{3/2}, \quad (2.53)$$

$$C_M = 0.06, \quad q^2 = \frac{1}{2} (\tilde{u}_k - \hat{u}_k)^2$$

where Γ is the blending function, $\nu_{T,RANS}$ is the kinematic eddy viscosity due to Menter, d is the wall distance function, S is the vorticity vector, and Δ is the cell volume. The blending function itself is computed as part of the flow, as follows:

$$\Gamma = \frac{1}{2} \left[1 - \tanh \left(5 \left(\frac{1}{\lambda_C^2} - 1 \right) + \phi \right) \right], \quad \phi = \tanh^{-1}(0.98) \quad (2.54)$$

$$\lambda_C = \alpha_1 \frac{\sqrt{\nu}}{C_\mu^{1/4} \sqrt{\kappa} d \sqrt{\omega}}, \quad C_\mu = 0.09 \quad (2.55)$$

The model constant α_1 is determined from analysis of the inflow boundary layer using Coles' law of the wall/wake and represents the point at which the wake law deviates from the log law[9]. This was fixed at $\alpha_1 = 24.55$ for the planar mixing layer case, and $\alpha_1 = 34.24$ for the sonic injection case.

Chapter 3

Numerical Formulation

This work employed NCSU's REACTMB code, which is a finite volume-based solver for the three dimensional, compressible Navier-Stokes equations with multi-component reacting gas chemistry. The inviscid fluxes are formulated with the Low Diffusion Flux-Splitting Scheme (LDFSS) of Edwards[10]. A higher-order extension is accomplished with Colella and Woodward's Piecewise Parabolic Method (PPM)[7], blended with a second-order central difference scheme via a switch developed by Ducros, et al[8]. Time discretization is accomplished with a second-order Crank-Nicholson scheme. A turbulence recycling/rescaling technique is used to generate and sustain large-scale turbulent structures in the flow.

3.1 Flux Discretization

In order to solve the flow system, the continuous governing equations are discretized over each cell volume, then solved using flux balancing. The integral form of the governing equations for a control volume V is given by:

$$\int_{\Omega} \frac{\partial U}{\partial t} d\Omega + \int_A E_j \cdot n_j dA = \int_{\Omega} S d\Omega \quad (3.1)$$

with the discrete form,

$$\Omega_c \frac{\partial U_c}{\partial t} + \sum_{k=1}^{nf,c} (E_j \cdot n_j)_{k,c} A_{k,c} = \Omega_c S_c \quad (3.2)$$

where c is a specific mesh cell, k is a face of that cell, Ω_c is the cell volume, A is the cell face area, and n is the outward normal. U is the vector of conservative variables for the fluid flow, E is the vector of fluxes of U , and S is a source term vector. For our set of governing equations,

U is given by:

$$U = \begin{bmatrix} \rho_1 \\ \rho \\ \rho u \\ \rho v \\ \rho w \\ \rho E_t \\ \rho k \\ \rho \omega \end{bmatrix} \quad (3.3)$$

The flux vector can be separated into a viscous and inviscid component. The viscous fluxes are discretized using a second-order central differencing scheme while the inviscid fluxes are discretized with LDFSS, as follows.

3.1.1 Low-Diffusion Flux Splitting Scheme (LDFSS)

LDFSS is a first order, Van Leer-type flux splitting scheme which formulates fluxes based on the physical characteristics of information flow into and out of the control volume[10]. The inviscid fluxes through a cell face are first split into convective and pressure terms,

$$E = A(\rho U E^c + p E^p) \quad (3.4)$$

where A is the cell face area and U is the velocity normal to the cell face,

$$U = un_x + vn_y + wn_z \quad (3.5)$$

and

$$E^c = \begin{bmatrix} Y_1 \\ 1 \\ u \\ v \\ w \\ H \\ k \\ \omega \end{bmatrix}, \quad E^p = \begin{bmatrix} 0 \\ 0 \\ n_x \\ n_y \\ n_z \\ 0 \\ 0 \\ 0 \end{bmatrix} \quad (3.6)$$

At the cell interface, the convective flux is defined as follows:

$$E_{1/2}^c = a_{1/2} [\rho_L C^+ E_L^c + \rho_R C^- E_R^c] \quad (3.7)$$

where L and R denote left and right cell states. The interface sound speed is

$$a_{1/2} = \frac{1}{2}(a_L + a_R) \quad (3.8)$$

and

$$C^+ = C_{VL}^+ - M_{1/2}^+ \quad (3.9)$$

$$C^- = C_{VL}^- + M_{1/2}^- \quad (3.10)$$

where

$$C_{VL}^+ = \alpha_L^+(1.0 + \beta_L)M_L - \beta_L M_L^+ \quad (3.11)$$

$$C_{VL}^- = \alpha_R^-(1.0 + \beta_R)M_R - \beta_R M_R^- \quad (3.12)$$

$$M_{1/2}^+ = M_{1/2} \left(\frac{2p_R}{p_L + p_R} - \delta \frac{|p_L - p_R|}{p_L} \right) \quad (3.13)$$

$$M_{1/2}^- = M_{1/2} \left(\frac{2p_L}{p_L + p_R} - \delta \frac{|p_L - p_R|}{p_R} \right) \quad (3.14)$$

and

$$\alpha_{L,R}^\pm = \frac{1}{2}[1.0 \pm \text{sign}(M_{L,R})] \quad (3.15)$$

$$\beta_{L,R} = -\max[0.0, 1.0 - \text{int}(|M_{L,R}|)] \quad (3.16)$$

$$M_{L,R}^\pm = \pm \frac{1}{4}(M_{L,R} \pm 1.0)^2 \quad (3.17)$$

$$M_{1/2} = \frac{1}{4}\beta_L\beta_R \left(\sqrt{\frac{1}{2}(M_L^2 + M_R^2)} - 1.0 \right)^2 \quad (3.18)$$

In the above, the interface Mach number is defined simply as

$$M_{L,R} = \frac{1}{a_{1/2}} [n_x u_{L,R} + n_y v_{L,R} + n_z w_{L,R}]. \quad (3.19)$$

The pressure component of the inviscid flux is defined:

$$E_{1/2}^p = E^p [D_L^+ p_L + D_R^- p_R] \quad (3.20)$$

where

$$D_{L,R}^\pm = \alpha_{L,R}^\pm(1.0 + \beta_{L,R}) - \beta_{L,R} P_{L,R}^\pm \quad (3.21)$$

and

$$P_{L,R}^\pm = \frac{1}{4}(M_{L,R} \pm 1.0)^2(2.0 \mp M_{L,R}). \quad (3.22)$$

3.1.2 Piecewise Parabolic Method (LD-PPM)

The above flux formulation depends upon the state vectors \vec{U}_L and \vec{U}_R at the left and right sides of the cell interface. For a first-order accurate system, these would be taken as the values at the center of the cells. In this study, the flux discretization was extended to a higher order by using the Piecewise Parabolic Method (PPM)[7] to reconstruct the interface values.

Given state vectors $\vec{U}_{L,i+1/2}$ and $\vec{U}_{R,i-1/2}$ we first set the left and right values to fourth-order averaging operators, which produce a fourth-order central difference approximation to the fluxes:

$$\vec{U}_{L,i+1/2} = \vec{U}_{R,i-1/2} = \frac{7}{2}(\vec{U}_i + \vec{U}_{i+1}) = \frac{1}{12}(\vec{U}_{i+2} + \vec{U}_{i-1}) \quad (3.23)$$

The PPM then performs a cell-limiting procedure to enforce monotonicity:

if $sign[(\vec{U}_{L,i+1/2} - \vec{U}_i)(\vec{U}_i - \vec{U}_{R,i-1/2})] = -1$ **then**

$$\vec{U}_{L,i+1/2}^M = \vec{U}_{R,i-1/2}^M = \vec{U}_i$$

else

$$C = \vec{U}_{L,i+1/2} - \vec{U}_{R,i-1/2}$$

$$D = 6.0[\vec{U}_i - \frac{1}{2}(\vec{U}_{L,i+1/2} - \vec{U}_{R,i-1/2})]$$

if $DC > CC$ **then**

$$\vec{U}_{R,i-1/2}^M = 3\vec{U}_i = 2\vec{U}_{L,i+1/2}$$

else if $-CC > DC$ **then**

$$\vec{U}_{L,i+1/2}^M = 3\vec{U}_i = 2\vec{U}_{R,i-1/2}$$

end if

end if

This procedure sets the interface values to the cell center value if \vec{U}_i is a local maximum or minimum, and otherwise ensures that the interpolation parabola that connects the interface states with the state at the cell center is monotonically increasing or decreasing.

3.1.3 Ducros Switch

While a monotonic reconstruction scheme such as PPM ensures stability in shock-dominated flows, it can damp out resolved-scale turbulence in other regions of the flow. This study addressed this problem by using a blending function by Ducros, et al.[8] to shift the flux reconstruction to a fourth-order central difference scheme in areas of high vorticity. The blending function is defined as follows:

$$\Gamma_D = \frac{(\nabla \cdot \vec{u})^2}{(\nabla \cdot \vec{u})^2 + (\omega)^2 + \epsilon} \quad (3.24)$$

where \vec{u} is the velocity vector, $\omega = \nabla \times \vec{u}$ is the resolved vorticity and $\epsilon = 10^{-8}$ is a small constant to avoid division by zero in regions where the divergence and vorticity disappear. The value of this function approaches 0 in weakly compressible, turbulent regions and 1 in

shock-dominated regions. The value of the reconstructed flow states at cell interfaces is then determined by:

$$\vec{U}_{L,i+1/2} = (1 - \Gamma_D)\vec{U}_{L,i+1/2}^C + \Gamma_D\vec{U}_{L,i+1/2}^M \quad (3.25)$$

$$\vec{U}_{R,i-1/2} = (1 - \Gamma_D)\vec{U}_{R,i-1/2}^C + \Gamma_D\vec{U}_{R,i-1/2}^M \quad (3.26)$$

where \vec{U}^C is the fourth-order central differenced value and \vec{U}^M is the value obtained via PPM. To avoid destabilizing the solution, the Ducros switch is only engaged after the simulation has progressed through several thousand iterations.

3.2 Time Intergation

To propagate the flow solution in time, a Crank-Nicholson time discretization was employed. The unsteady residual R is formed as follows:

$$R^{n+1,k} = \frac{U^{n+1,k} - U^n}{\Delta t} + \frac{1}{2} \left(R(U^{n+1,k}) + R(U^n) \right) \quad (3.27)$$

where U is the conservative variable vector, the superscripts n and $n + 1$ represent the current and next time level, and k is the current sub-iteration level. For each time step, the solution is iterated in k to a desired convergence. The residual at each sub-iteration is updates as follows, for a single grid point:

$$\begin{aligned} -R_{i,j,k}^{n+1,k} = & \left[\frac{1}{\Delta t} \frac{\partial U}{\partial V} + \frac{1}{2} \left(\tilde{A} - \frac{\partial S}{\partial V} \right) \right]_{i,j,k}^{n+1,k} \Delta V_{i,j,k}^{n+1,k+1} + \\ & \frac{1}{2} \tilde{B} \Delta V_{i,j-1,k}^{n+1,k+1} + \frac{1}{2} \tilde{C} \Delta V_{i,j+1,k}^{n+1,k+1} + \\ & \frac{1}{2} \tilde{D} \Delta V_{i,j,k-1}^{n+1,k+1} + \frac{1}{2} \tilde{E} \Delta V_{i,j,k+1}^{n+1,k+1} + \\ & \frac{1}{2} \tilde{F} \Delta V_{i-1,j,k}^{n+1,k+1} + \frac{1}{2} \tilde{G} \Delta V_{i+1,j,k}^{n+1,k+1} \end{aligned} \quad (3.28)$$

where V is the primitive variable vector, S is the source term vector, and $\tilde{A} - \tilde{G}$ are the flux Jacobians, whose calculation is described in[10]. The system Jacobian matrix \tilde{A} is approximated with a symmetric planar Gauss-Seidel (SPGS) algorithm. Matrix elements in the same $i = const$ plane are denoted as D and defined as

$$D = \frac{1}{\Delta t} \frac{\partial U}{\partial V} + \frac{1}{2} \left(\tilde{A} - \frac{\partial S}{\partial V} + \tilde{B} + \tilde{C} + \tilde{D} + \tilde{E} \right) \quad (3.29)$$

while the off-plane components are grouped into

$$L = \tilde{F} \quad (3.30)$$

$$U = \tilde{G} \quad (3.31)$$

Then equation (3.30) can be rewritten as:

$$-R^{n+1,k} = (D + L)^{n+1,k} (D^{n+1,k})^{-1} (D + U)^{n+1,k} \Delta \vec{V}^{n+1,k+1} \quad (3.32)$$

The change in the primitive vector variable is then computed with a forward and backward sweep in the k-direction:

$$\text{forward: } \Delta \vec{V}_i^{n+1,k+1/2} = \left(D_i^{n+1,k} \right)^{-1} \left(-R_i^{n+1,k} - L_{i-1}^{n+1,k} - L_{i-1}^{n+1,k} \Delta \vec{V}_{i-1}^{n+1,k+1/2} \right) \quad (3.33)$$

$$\text{backward: } \Delta \vec{V}_i^{n+1,k+1} = \Delta \vec{V}_i^{n+1,k+1/2} - \left(D_i^{n+1,k} \right)^{-1} U_{i+1}^{n+1,k} \Delta \vec{V}_{i+1}^{n+1,k+1} \quad (3.34)$$

The block pentadiagonal matrix D is approximately solved using Incomplete Lower/Upper (ILU) factorization, defined as:

$$(L + D + U)^{n+1,k} \Delta \vec{V}^{n+1,k+1} = -R^{n+1,k} \quad (3.35)$$

Finally, the primitive variables are updated as follows:

$$\vec{V}^{n+1,k+1} = \vec{V}^{n+1,k} + \Delta \vec{V}^{n+1,k+1} \quad (3.36)$$

3.3 Turbulence Recycling/Re-scaling

To introduce and sustain large-scale turbulence in the flow, a turbulence recycling/rescaling technique is used, as described in detail by Boles, et al.[9] A 'recycle plane' is chosen where the fluctuations in velocity, density, and temperature are extracted by subtracting the instantaneous flow profile from a time- and span-averaged profile. These fluctuation quantities are then rescaled according to boundary layer similarity laws and superimposed onto a RANS mean inflow profile, upstream of the recycling plane.

Chapter 4

LES/RANS Simulations of Planar Mixing Layer

4.1 Calculation Details

To evaluate the scalar mixing models, a numerical experiment based on that of Barre, et. al was performed to simulate planar shear mixing of two high-speed gas streams. First, a simulation of a supersonic air stream mixing with a subsonic airstream was conducted, with conditions matching those of the Barre, et al. experiment[1]. The subsonic air stream was then replaced with a subsonic argon stream, and a supersonic helium stream. The convective Mach number, defined as $M_c = \Delta U / (a_1 + a_2)$, was kept close to 0.6 for each case to attempt to match the shear layer spreading rates.

The layout of the experiment is shown in Figure 6.1. In the top inflow region, a stream of supersonic air develops over a flat plate, reaching a boundary layer thickness of 1cm at edge of the splitter plate. The lower gas stream in the physical experiment passes through several screens to homogenise the flow; for the purposes of the numerical experiment, it was assumed that this flow was laminar and so the inflow region was not modeled. The effects of the 10 degree angle of the splitter plate itself was modeled by adding an upward 10 degree angle in the lower gas flow near the splitter plate.

The two gas streams mix in the region of interest, with the last measurement station located at 0.3 meters. Beyond this is a 0.4 m buffer region. One complication in simulating this experiment was the influence of the outflow boundary condition on the subsonic part of the mixing layer: pressure changes would propagate upstream, causing deflection of the mixing layer. To correct this, a slope was added to the bottom surface of the buffer region, with an angle determined by trial and error via RANS simulations so as to maintain pressure matching between the two gas streams. The optimal angle was found to be 12.6 degrees for air/air mixing,

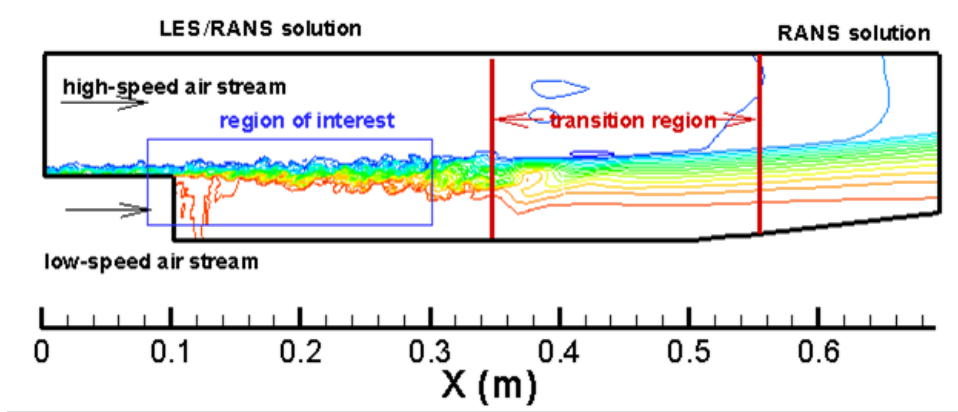


Figure 4.1: Schematic of computational domain (Barre, et al. experiment)

and 10.3 degrees for air/argon mixing. For the case of helium mixing with air, both gas streams were supersonic and the slope was not needed.

Each case was first simulated using RANS in a 2-D domain. These solutions were then used to initialize the LES/RANS simulations, which used a full 3-D grid consisting of 80 blocks and 9.624 million cells. The spanwise extent of the grid used in the LES/RANS simulation was set at 0.12m (about 4.8 shear layer widths at the last measurement station), with periodic boundary conditions at the side walls. One issue with the LES/RANS simulations was flow separation near the outflow, which created a pressure imbalance between the two gas streams and in some cases caused backflow into the domain from the outflow boundary. To address this, the solution in the buffer region was forced to match the initial RANS solution, with a blending function ψ defining the transition between the two models:

$$\bar{x} = \max(0, \min(1, \frac{X - 0.35}{0.2})) \quad (4.1)$$

$$\psi = 2\bar{x}^3 - 3\bar{x}^2 + 1 \quad (4.2)$$

where X is the axial distance from the tip of the splitter plate. The blending function was then used to modify the residual of the equation system at each sub-iteration:

$$\vec{R}_{buf}^{n+1,k} = \psi \vec{R}^{n+1,k} + (1 - \psi) \frac{\Omega}{\Delta t} (\vec{Q}^{n+1,k} - \vec{Q}_{RANS}) \quad (4.3)$$

where Ω is the cell volume, Δt is the time step, \vec{Q} is the local solution, and \vec{Q}_{RANS} is the RANS solution.

Table 1 lists the flow conditions for each of the three simulations. The simulations represent a time of around 0.01 seconds, or 6 flowthrough times through the measured region for the air

Table 4.1: Simulated Flow Conditions

	$U_1(m/s)$	$U_2(m/s)$	$P_1(Pa)$	$P_2(Pa)$	$T_1(K)$	$T_2(K)$	$a_1(m/s)$	$a_2(m/s)$	M_c
Air-Air	481	101	11300	11300	180	286	269	337	0.62
Air-Argon	481	101	11300	11300	180	286	269	315	0.65
Air-Helium	481	1201	11300	12400	180	250	269	931	0.60

and argon streams. Statistics necessary for mixing model assessment were gathered for the last 2/3 of each simulation.

4.2 Comparison with Experiment

In this section, the results of the air/air mixing simulation are compared with the experiment of Barre, et al. Figure 6.2 shows a snapshot of the measured region of the mixing layer. The turbulent boundary layer developed in the inflow region sustains gas mixing inside the shear layer, which spreads downstream along the centerline of the domain. The pressure of the two gas stream remains evenly matched, with spikes and troughs occurring locally in the eddies. Figure 6.5 shows velocity profiles taken at different measurement stations in the flow (the scale of each large tick mark is 600 m/s). The results generated by the RANS and LES/RANS simulations are almost identical. In both cases, the velocity profiles immediately downstream of the splitter plate match the experiment very closely, but farther downstream the shear layer spreading rate begins to exceed that seen in the experiment. This is seen in Figure 6.6, which compares the simulated and experimental spreading rates. Here, the shear layer thickness is defined as $\delta = y_1 - y_2$, where y_1 is the point where $U = U_2 + 0.9^{1/2}(U_1 - U_2)$ and y_2 is where $U = 0.1^{1/2}(U_1 - U_2)$. The spreading rate taken from the LES/RANS data closely matches the slope of the Stanford Curve as presented in Barre, et al's paper, which was compiled from an average of multiple similar experiments in literature.

Figure 6.7 and Figure 6.8 show the *rms* axial velocity fluctuation profiles, with y values normalized by the shear layer width. Generally, the results are in good agreement with the experiment. Near the splitter plate, the velocity fluctuations in the lower stream are under-predicted due to the omission of turbulence in the lower air stream which was clearly present , though not measured, in the Barre, et al. experiment. This discrepancy becomes less significant in the downstream measurement stations.

Figure 6.9 shows the Reynolds shear stress profile taken 180mm downstream of the splitter plate. The data presented by Barre, et al. were estimated from velocity gradient data and an

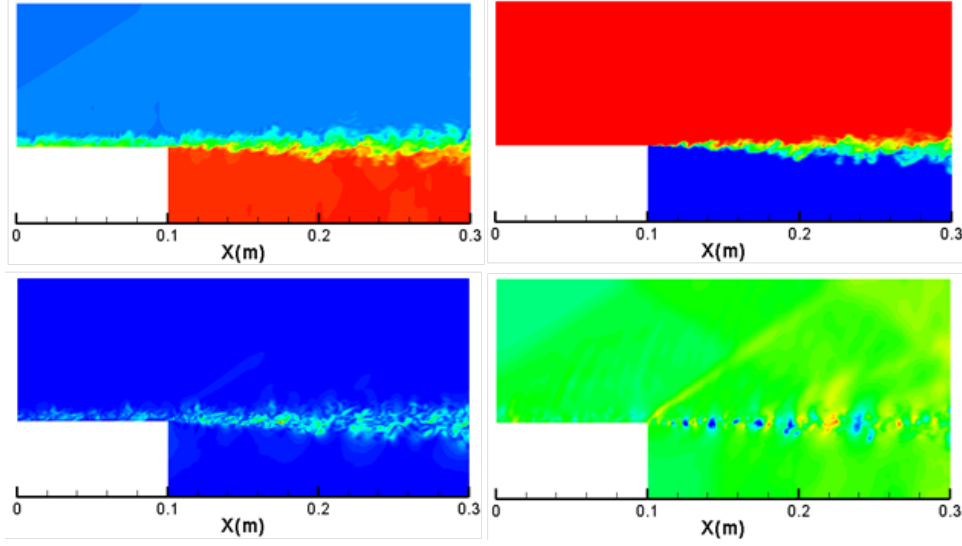


Figure 4.2: Snapshots from simulation of Barre, et al. mixing layer (clockwise from upper left: temperature, mass fraction, transverse velocity, pressure)

assumed mixing length; the two curves offer high and low estimates. The LES/RANS Reynolds stresses are nearly double those of the experiment; however, the peak value of 0.0078 is in very good agreement with the data from other shear layer experiments presented in Figures 19 and 20 of Barre, et al's paper. Their own peak value of about 0.004 is below most of this data, so we can assume that the stresses predicted by our simulation are reasonable. Finally, Figure 6.10 compares the *rms* temperature fluctuations at the downstream measurement stations. While the peak values are in good agreement with those of the experiment, the shape of the distribution is somewhat wider in the simulation, especially in the lower gas stream. This could be due to the higher mixing layer spreading rate in the LES/RANS simulation.

Overall, the agreement with the physical experiment is good, and the data from the simulations can be used to evaluate turbulent mixing models.

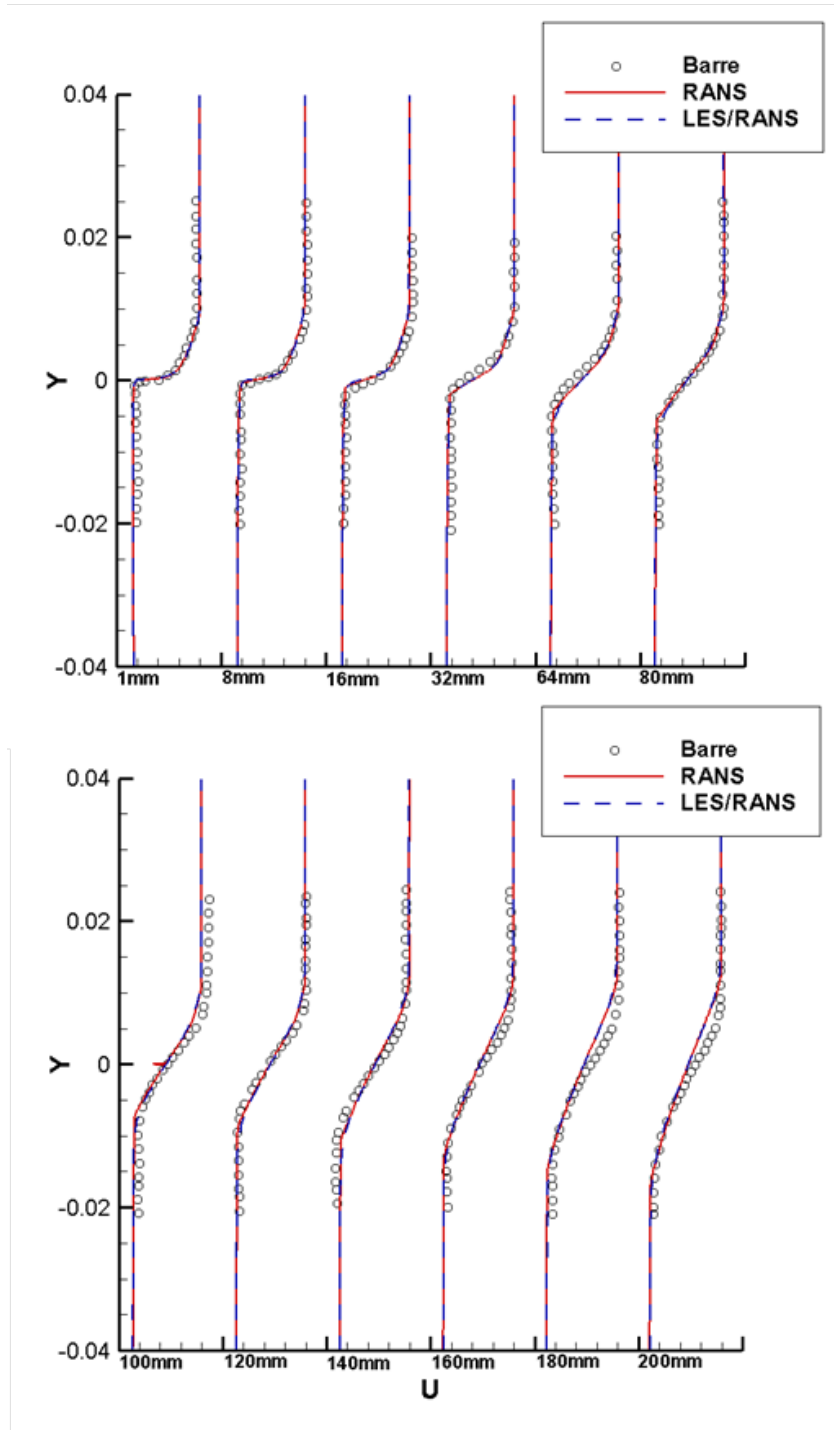


Figure 4.3: Velocity profiles at different axial stations (Barre, et al. experiment)

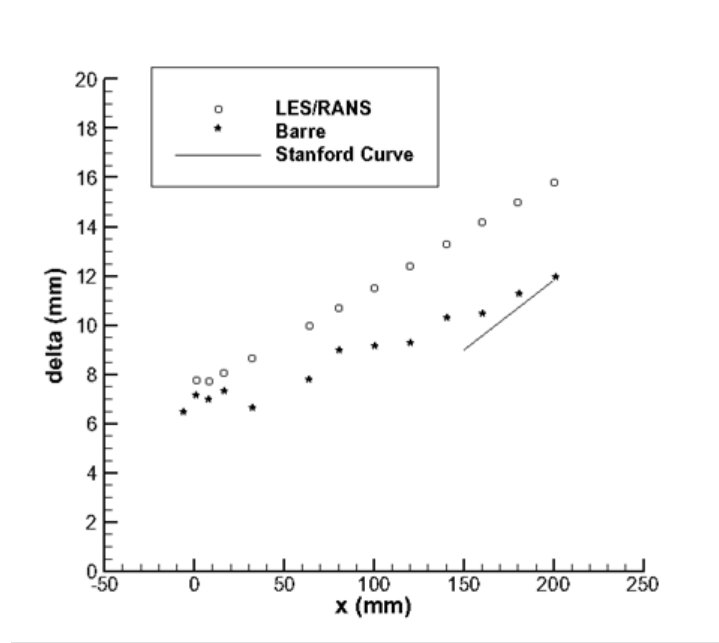


Figure 4.4: Mixing layer spreading rate (Barre, et al. experiment)

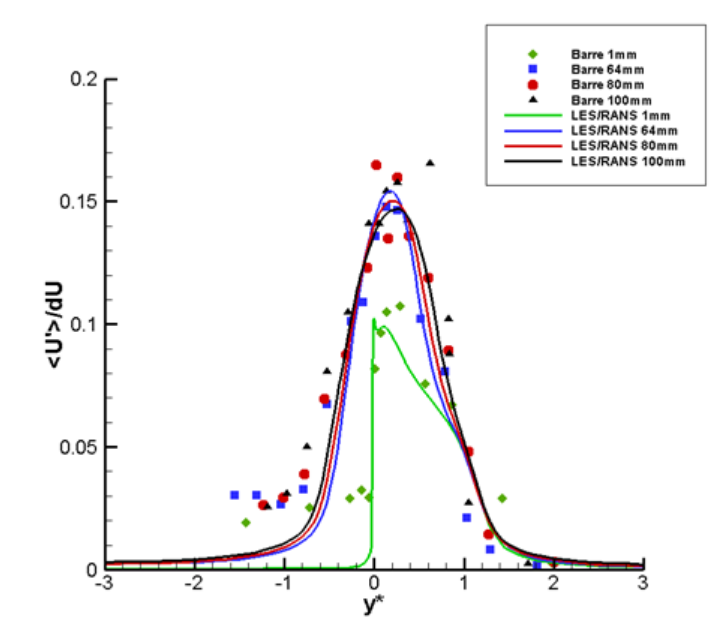


Figure 4.5: rms axial velocity fluctuation intensity profiles (near-field stations)

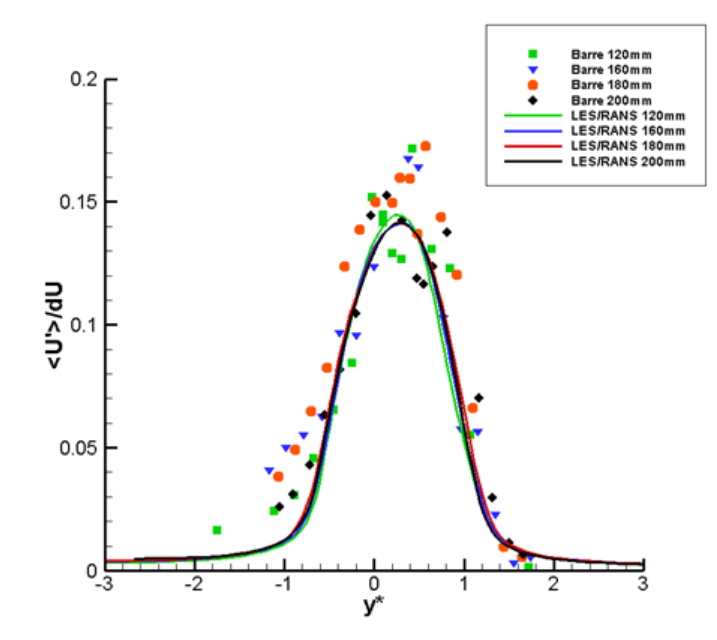


Figure 4.6: rms axial velocity fluctuation intensity profiles (far-field stations)

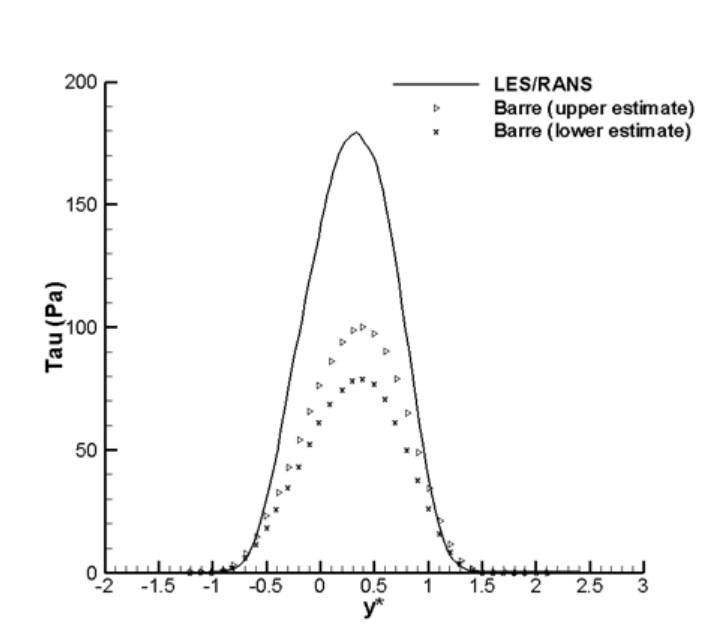


Figure 4.7: Resolved Reynolds shear stress versus predictions deduced by Barre, et al.

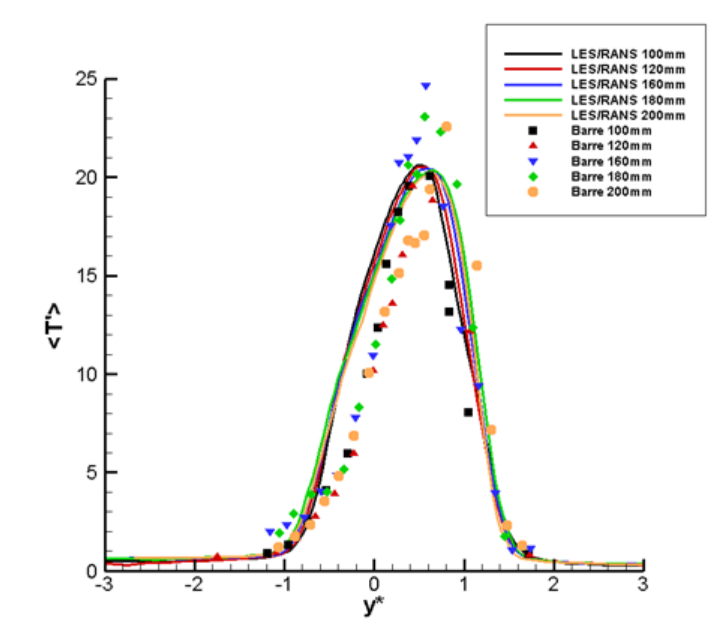


Figure 4.8: rms temperature fluctuation predictions (K) versus experimental data

Chapter 5

Model Evaluation

5.1 Data Extraction

In order to evaluate the turbulent mixing models of Brinckman, et al. and Xiao, et al., fluctuation statistics were extracted from the LES/RANS data through ensemble averaging during the last portion of the simulation. This data was also used to calculate exact expressions for the modeled terms so that the LES/RANS simulation could be used as a 'truth model' for mixing model evaluation. Thus, the resolved Reynolds stress tensor was calculated as follows:

$$\overline{\rho u_i'' u_j''} = \overline{\rho u_i u_j} - \frac{\overline{\rho u_i} \overline{\rho u_j}}{\bar{\rho}} \quad (5.1)$$

similarly, the turbulent scalar flux was evaluated as:

$$\overline{\rho u_j'' Y''} = \overline{\rho u_j Y} - \frac{\overline{\rho u_j} \overline{\rho Y}}{\bar{\rho}} \quad (5.2)$$

and the concentration variance σ was calculated as

$$\bar{\rho} \sigma = \overline{\rho Y'' Y''} = \overline{\rho Y^2} - \frac{\overline{\rho Y} \overline{\rho Y}}{\bar{\rho}} \quad (5.3)$$

Here, the overbar denotes time and span-average quantities, while Favre-averaged quantities are denoted with a tilde as \tilde{Q} , where $\tilde{Q} = \frac{\overline{\rho Q}}{\bar{\rho}}$. These resolved-scale quantities can be used to infer other terms in RANS-level modeling, by utilizing various RANS closure assumptions for turbulent stress and scalar flux. for instance, using the Boussinesq hypothesis,

$$\bar{\rho} \nu_{t,M} = \frac{\left(-\overline{\rho u_i'' u_j''} + \frac{2}{3} \overline{\rho k} \delta_{ij} \right) \frac{\partial \tilde{u}_i}{\partial x_j}}{\max \left[\left(\frac{\partial \tilde{u}_i}{\partial x_j} + \frac{\partial \tilde{u}_j}{\partial x_i} - \frac{2}{3} \delta_{ij} \frac{\partial \tilde{u}_k}{\partial x_k} \right) \frac{\partial \tilde{u}_i}{\partial x_j}, \alpha_M \right]} \quad (5.4)$$

$$\overline{\rho k} = \frac{1}{2} \left(\overline{\rho u_k u_k} - \frac{\overline{\rho u_k} \overline{\rho u_k}}{\bar{\rho}} \right) \quad (5.5)$$

we can determine the momentum eddy viscosity $\nu_{t,M}$. Similarly, we can determine an eddy viscosity characteristic of turbulent mass transport by utilizing a gradient-diffusion model for the turbulent scalar flux:

$$\bar{\rho} \nu_{t,S} = \frac{-\overline{\rho u_j'' Y''} \frac{\partial \tilde{Y}}{\partial x_j}}{\max \left[\frac{\partial \tilde{Y}}{\partial x_j} \frac{\partial \tilde{Y}}{\partial x_j}, \alpha_S \right]} \quad (5.6)$$

In the above equations, α_M and α_S are small constants added to prevent division by zero; in the current analysis, they are defined as $\alpha_M = 1 \times 10^{-5} (\tilde{u}/\Delta)^2$ and $\alpha_S = 1 \times 10^{-5}/\Delta^2$, with $\Delta = 0.001m$. We can then use these viscosities to estimate the turbulent Schmidt number,

$$Sc_t = \frac{\nu_{t,M}}{\nu_{t,S}} \quad (5.7)$$

Because $\nu_{t,S}$ can be very small where mean flow gradients are zero, Sc_t is set to zero if the concentration variance σ is less than 1×10^{-4} . Figures 5.1 - 5.3 plot the turbulent Schmidt number at different stations for each of the three mixing-layer simulations. The profiles at each station have been shifted by 0.5 m for visual clarity. In each case, the values near the center of the mixing layer approach between 0.7 and 0.8 regardless of the gas composition. Near the edge of the mixing layers, the results become very sensitive to small gradients, creating spikes, especially in the air-helium data. The accuracy of this edge data is questionable, but overall we can see that the Schmidt number for these mixing layers is not constant, as is often assumed in RANS modeling.

The scalar dissipation rate ϵ_S , which is employed in both of the mixing models examined, can be estimated by balancing the concentration variance equations:

$$\underbrace{2\bar{\rho}\epsilon_S}_{\text{dissipation}} = \underbrace{-2\overline{\rho u_i'' Y''} \frac{\partial \tilde{Y}}{\partial x_j}}_{\text{production}} + \underbrace{\frac{\partial}{\partial x_j} \left[\rho D \frac{\partial \sigma}{\partial x_j} - \overline{\rho u_j'' (Y'')^2} \right]}_{\text{molecular and turbulent diffusion}} - \underbrace{\frac{\partial \bar{\rho} \sigma}{\partial t} - \frac{\partial \bar{\rho} \sigma \tilde{u}_j}{\partial x_j}}_{\text{convection}} \quad (5.8)$$

If we neglect molecular diffusion and evaluate the turbulent diffusion term using Favre averaging as above, this becomes

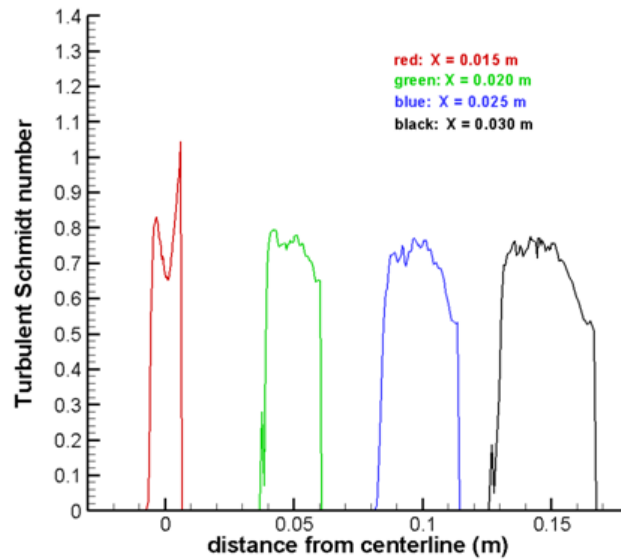


Figure 5.1: Turbulent Schmidt number profiles (air-air mixing)

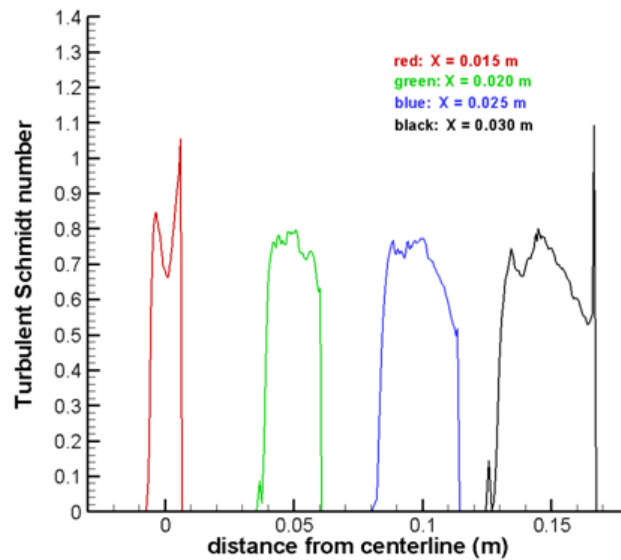


Figure 5.2: Turbulent Schmidt number profiles (air-argon mixing)

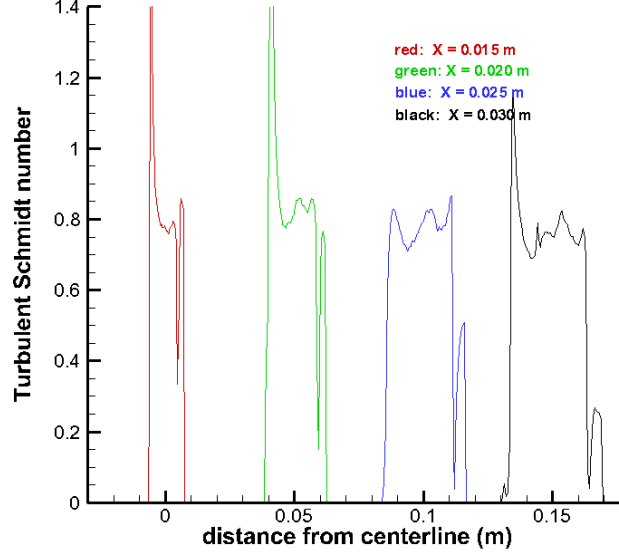


Figure 5.3: Turbulent Schmidt number profiles (air-helium mixing)

$$\underbrace{2\bar{\rho}\epsilon_S}_{\text{dissipation}} = \underbrace{-2\bar{\rho}u_i''Y''\frac{\partial\tilde{Y}}{\partial x_j}}_{\text{production}} - \underbrace{\frac{\partial}{\partial x_j}\left[\bar{\rho}u_jY^2 - 2\bar{\rho}u_jY\frac{\bar{\rho}Y}{\bar{\rho}} + 2\left(\frac{\bar{\rho}Y}{\bar{\rho}}\right)^2\frac{\bar{\rho}u_j}{\bar{\rho}} - \bar{\rho}Y^2\frac{\bar{\rho}u_j}{\bar{\rho}}\right]}_{\text{turbulent diffusion}} - \underbrace{\frac{\partial\bar{\rho}\sigma}{\partial t} - \frac{\partial\bar{\rho}\sigma\tilde{u}_j}{\partial x_j}}_{\text{convection}} \quad (5.9)$$

This can be evaluated by substituting in expressions for the turbulent scalar flux and concentration variance, and calculating derivatives from mean flow data using finite volume methods. Figure 5.4 - Figure 5.6 show each term of the above equation at different measurement stations for each of the three simulated flows. Again, profiles have been shifted 0.05 m along the x-axis for visual clarity. For the air-air and air-argon mixing cases, the diffusion and convection terms nearly cancel out, meaning that the scalar dissipation rate is roughly equal to the scalar production rate. This is largely true for the air-helium mixing case, although the balance of the terms inside the mixing layer is skewed due to the fact that the helium stream is also supersonic.

5.2 Model Form Evaluation

Having obtained estimates for the scalar dissipation rate and concentration variance, we can now evaluate the models for the turbulent diffusivity $\nu_{t,S}$ of Brinckman, et al. and Xiao, et al.

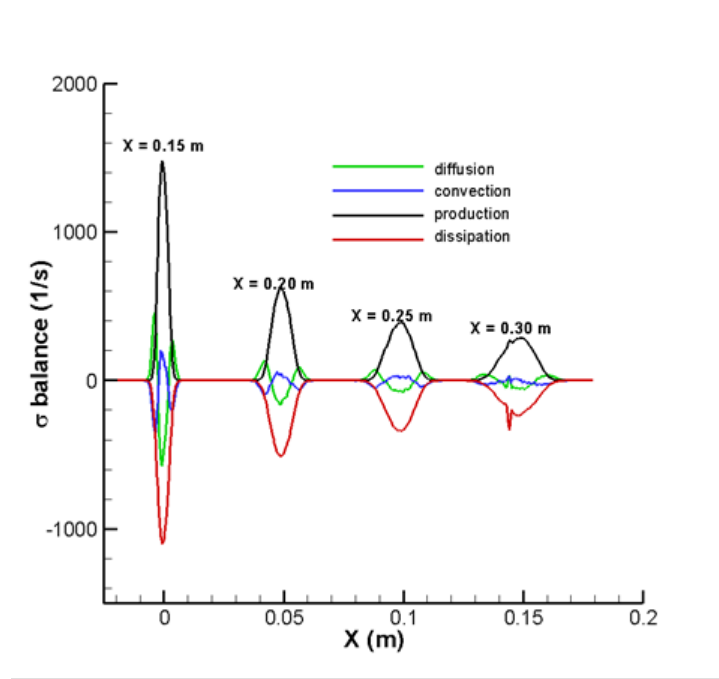


Figure 5.4: scalar fluctuation energy balance (air-air mixing)

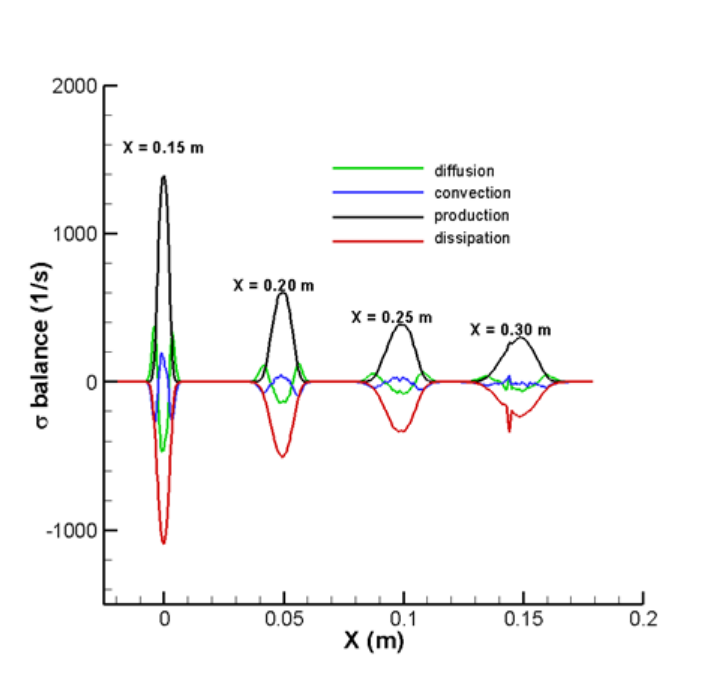


Figure 5.5: Scalar fluctuation energy balance (air-argon mixing)

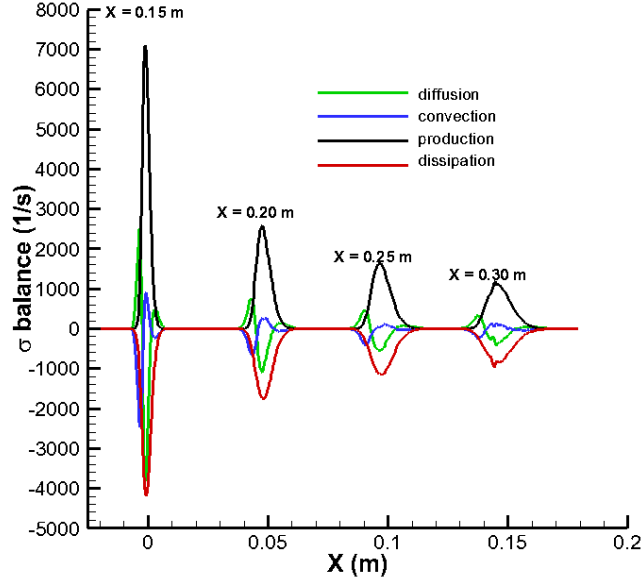


Figure 5.6: Scalar fluctuation energy balance (air-helium mixing)

Brinckman, et al. define the turbulent diffusivity as

$$\nu_{t,S(B)} = C_X k \sqrt{\frac{k\sigma}{\epsilon\epsilon_S}}, \quad C_X = 0.14 \quad (5.10)$$

while Xiao, et al. define it as

$$\nu_{t,S(X)} = \nu_{t,M} + C_Y k \frac{\sigma}{\epsilon_S}, \quad C_Y = 0.0325 \quad (5.11)$$

These equations can be evaluated using previously derived terms from LES/RANS data and compared with the form of $\nu_{t,S}$ defined in Eq. 5.6. Additionally, Brinckman, et al.'s model used the turbulent dissipation rate ϵ , which could normally be inferred from the LES/RANS data through detailed balancing. However, the necessary statistics for such analysis were not collected in the present work, so this expression was modeled using

$$\epsilon = 0.09 \frac{k^2}{\nu_{t,M}} \quad (5.12)$$

Figure 5.7 - Figure 5.9 compare the two modeled mass diffusivities with the form obtained in Eq. 5.6. for the three simulated mixing experiments. The profile shapes are matched closely by both of the models; however, the model of Brinckman, et al. consistently overpredicts the

peak mass diffusivity in each of the three cases. The model of Xiao, et al., shows very good agreement with the LES/RANS results overall. This can be attributed to the inclusion of the momentum eddy viscosity in the form of the model, which ensures that the mass diffusivity will not vanish in areas of low concentration fluctuation. In essence, under the model of Xiao et al. the concentration variance and scalar dissipation provide a correction to the mass diffusivity. This same form can be applied to the model of Brinckman, et al., and the coefficient in both models can be adjusted to provide an 'optimized' form, as follows:

$$\nu_{t,S(X)_{Opt}} = \nu_{t,M} + C_{Y,opt} k \frac{\sigma}{\epsilon_S}, \quad C_{Y,opt} = 0.0253 \quad (5.13)$$

$$\nu_{t,S(B)_{Opt}} = \nu_{t,M} + C_{X,opt} k \sqrt{\frac{k\sigma}{\epsilon\epsilon_S}}, \quad C_{X,opt} = 0.0260 \quad (5.14)$$

The optimal coefficients were determined for each case and profile by matching the exact scalar variance production rate, $P_s = -\overline{\rho u_i'' Y''} \frac{\partial \tilde{Y}}{\partial x_j}$ with the modeled form, $P_{s,mod} = \bar{\rho} \nu_{S,opt} \frac{\partial \tilde{Y}}{\partial x_j} \frac{\partial \tilde{Y}}{\partial x_j}$. Figure 5.10 - Figure 5.12 show the optimized forms of the scalar variance production rate compared to the exact value for each mixing case, with very good agreement reached for all cases.

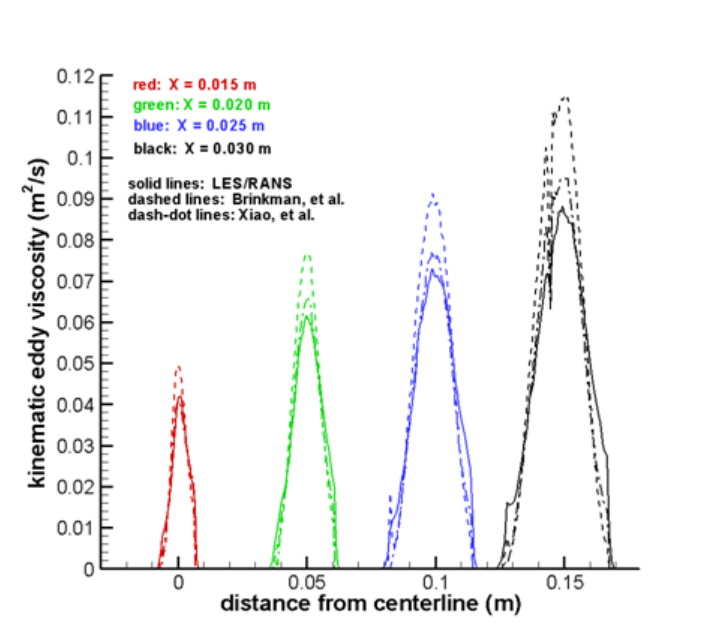


Figure 5.7: Mass diffusivities predicted by different models (air-air mixing)

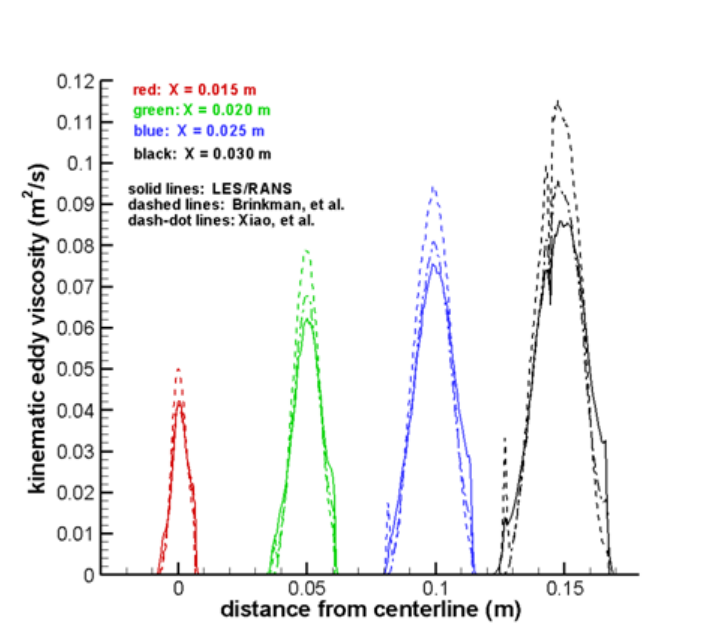


Figure 5.8: Mass diffusivities predicted by different models (air-argon mixing)

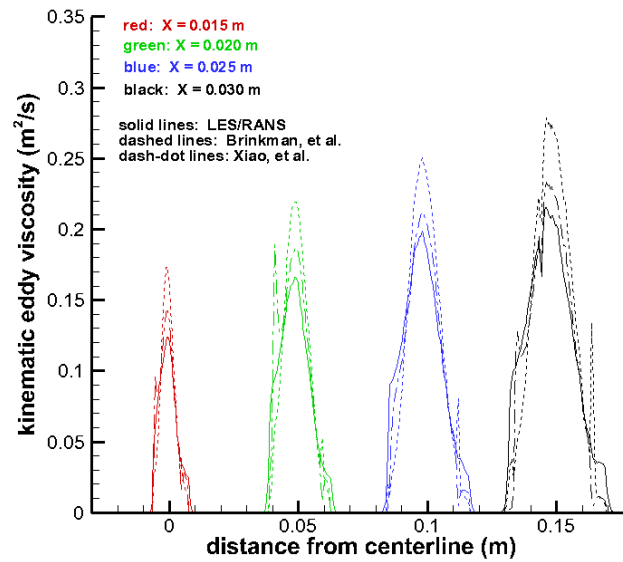


Figure 5.9: Mass diffusivities predicted by different models (air-helium mixing)

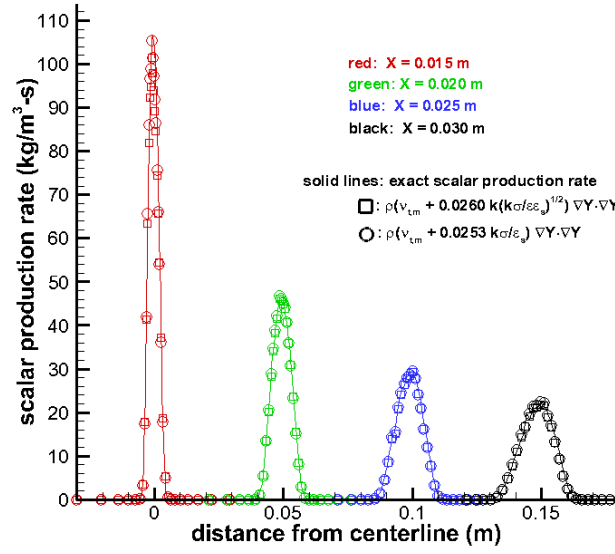


Figure 5.10: Scalar production rates predicted by different 'optimized' models (air-air mixing)

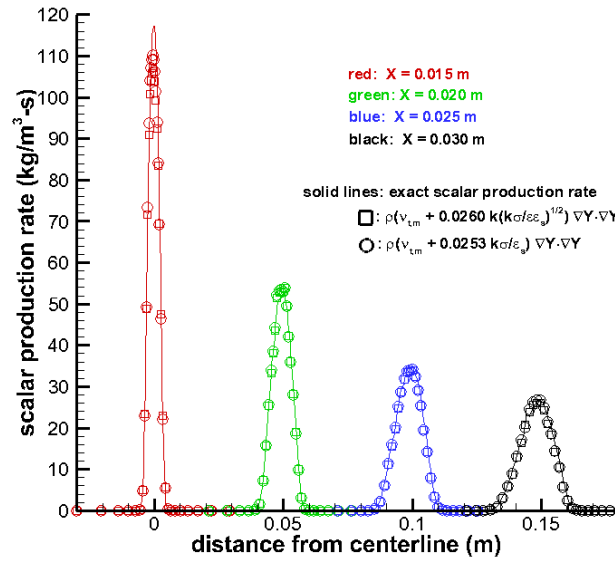


Figure 5.11: Scalar production rates predicted by different 'optimized' models (air-argon mixing)

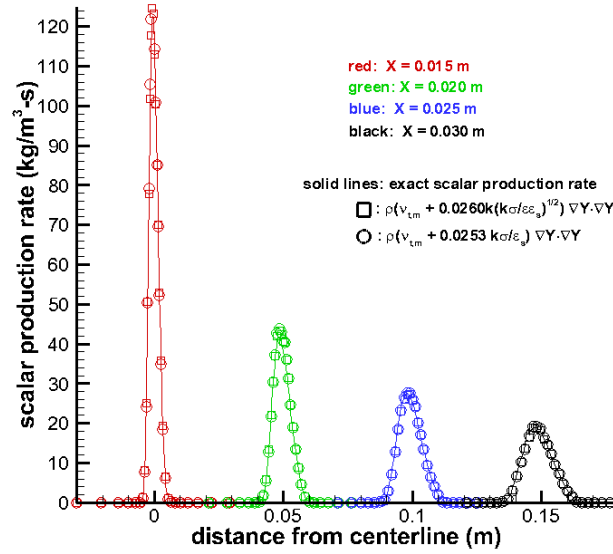


Figure 5.12: Scalar production rates predicted by different 'optimized' models (air-helium mixing)

In order to use the modeled forms of the mass diffusivity with RANS, it is necessary to model the constituent components involved in the models of Xiao, et al. and Brinckman, et al. Hence it was desired to evaluate their models for the scalar dissipation rate ϵ_S . The transport equation for the scalar dissipation rate according to Brinckman, et al. is

$$\frac{\partial \bar{\rho} \epsilon_S}{\partial t} + \frac{\partial \bar{\rho} \epsilon_S \tilde{u}_j}{\partial x_j} = \frac{\partial}{\partial x_j} \left[\rho \left(\frac{\nu}{Sc} + \frac{\nu_{t,S}}{\sigma_{\epsilon_S}} \right) \frac{\partial \epsilon_S}{\partial x_j} \right] + P_s \left(C_{d1} \frac{\epsilon_S}{\sigma} + C_{d2} \frac{\epsilon}{k} \right) + C_{d3} P_k \frac{\epsilon_S}{k} - \left(C_{d4} \frac{\epsilon_S}{\sigma} + C_{d5} \frac{\epsilon}{k} \right) \bar{\rho} \epsilon_S \quad (5.15)$$

while that of Xiao, et. al is

$$\frac{\partial \bar{\rho} \epsilon_S}{\partial t} + \frac{\partial \bar{\rho} \epsilon_S \tilde{u}_j}{\partial x_j} = \frac{\partial}{\partial x_j} \left[\rho \left(\frac{\nu}{Sc} + C_{Y5} \nu_{t,S} \right) \frac{\partial \epsilon_S}{\partial x_j} \right] + C_{Y6} P_s \frac{\epsilon_S}{\sigma} + 2 \frac{\epsilon_S}{k} \left[C_{Y2} P_k + \frac{2C_{Y2} + 1}{3} \bar{\rho} k \frac{\partial \tilde{u}_k}{\partial x_k} \right] - C_{Y7} \bar{\rho} \epsilon_S \frac{\epsilon_S}{\sigma} + C_{Y6} \bar{\rho} \frac{\nu}{Sc} \nu_{t,S} \left(\frac{\partial^2 \tilde{Y}}{\partial x_k \partial x_k} \right)^2 \quad (5.16)$$

Because Xiao, et al,'s formulation is written to solve for the sum of the concentration variances and scalar dissipation rates of all species, it is necessary to divide both values by two (for a binary mixture) to have values comparable to those of Brinckman, et al. For both models,

the production rates of turbulent kinetic energy and scalar fluctuation energy are defined as

$$P_k = -\overline{\rho u_i'' u_j''} \frac{\partial \tilde{u}_i}{\partial x_j} \quad (5.17)$$

$$P_s = -\overline{\rho u_i'' Y''} \frac{\partial \tilde{Y}}{\partial x_j} \quad (5.18)$$

Equations 5.15 and 5.16 can now both be solved for the scalar dissipation rate by using the values of P_k , P_s , k , σ , $\nu_{t,S}$, and ϵ extracted from the mean flow data from the LES/RANS simulation. In the present work, this was accomplished by modifying to RANS solver to evolve the modeled forms of ϵ_S taken from the above equations while taking the other variables from the LES/RANS solution as constants. Figure 5.13 and Figure 5.14 compare the modeled forms of scalar dissipation with the 'exact' solution derived from detailed balancing (Eq. 5.8). Figure 5.13 plots the different forms of scalar dissipation for each of the three flow cases, extracted along the line of greatest dissipation (nominally the center of the shear layer, $y=0$). Figure 5.14 plots profile data taken at $x=0.25$ m from the splitter plate. In the far field, both models predict the scalar dissipation rate for the air-argon and air-air mixing cases with good accuracy. There is more deviation in the air-helium mixing case, with the model of Brinkman, et al. overpredicting with peak dissipation rate by a large margin, and the model of Xiao, et al. underpredicting it. The former result is explained by looking at Figure 5.13; the Brinckman model matches the profile shape, but with an offset in the x -direction. Consequently, the peak values of scalar dissipation are shifted forward in the flow, causing overprediction of the dissipation rate for all stations in the far field. On the other hand, in the air-air and air-argon mixing cases, the peak dissipation rates in the upstream portion of the mixing layer are severely underpredicted by both models, before leveling out to match the 'real' values farther downstream. This suggests that both models function poorly in the presence of high concentration gradients.

Similarly, we also wish to evaluate the modeled form of the concentration variance σ . For Brinckman, et al. and Xiao, et al., the modeled transport equation is:

$$\frac{\partial(\bar{\rho}\sigma)}{\partial t} + \frac{\partial(\bar{\rho}\tilde{u}_j\sigma)}{\partial x_j} = \frac{\partial}{\partial x_j} \left[\bar{\rho} \left(\frac{\nu}{Sc} + \frac{\nu_{t,S}}{\sigma_s} \right) \frac{\partial \sigma}{\partial x_j} \right] + P_s \left(\frac{\partial \tilde{Y}}{\partial x_j} \right)^2 - 2\bar{\rho}\epsilon_S \quad (5.19)$$

where σ_s is a model constant equaling 1.0. As for the modeled scalar dissipation, the transport equation was incorporated into the RANS solver, with all of the values except σ itself taken from the LES/RANS data. The modeled and actual concentration variance for each flow extracted from the flow centerline is shown in Figure 5.15. For the air-air and air-argon mixing cases, the modeled concentration variance matches the exact results surprisingly closely in the near-field. However, the model overpredicts the variance for both cases in the far-field. For the helium

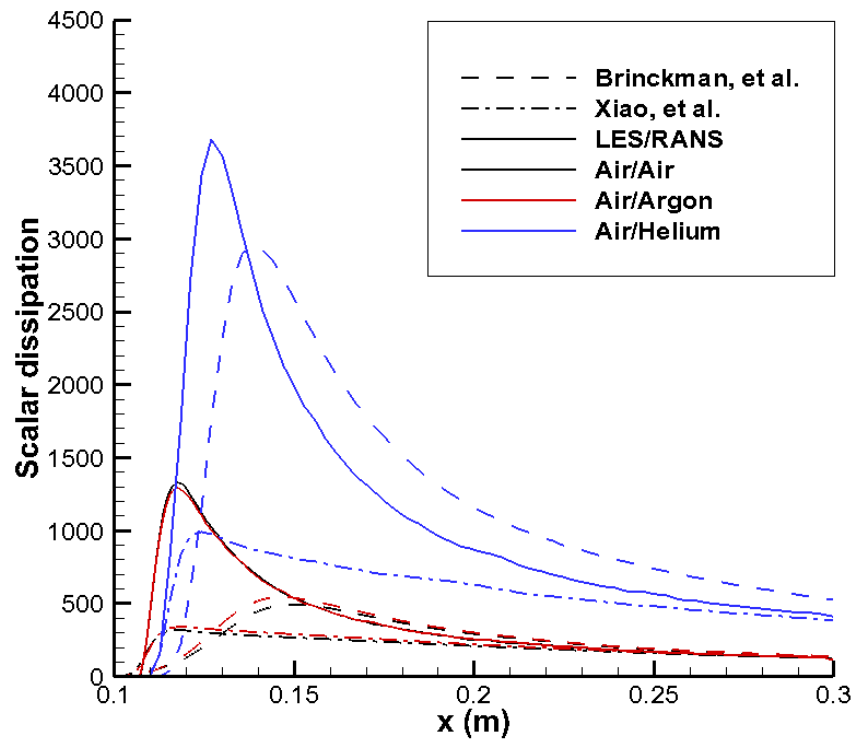


Figure 5.13: Scalar dissipation rates predicted by different models extracted along line of peak dissipation rates

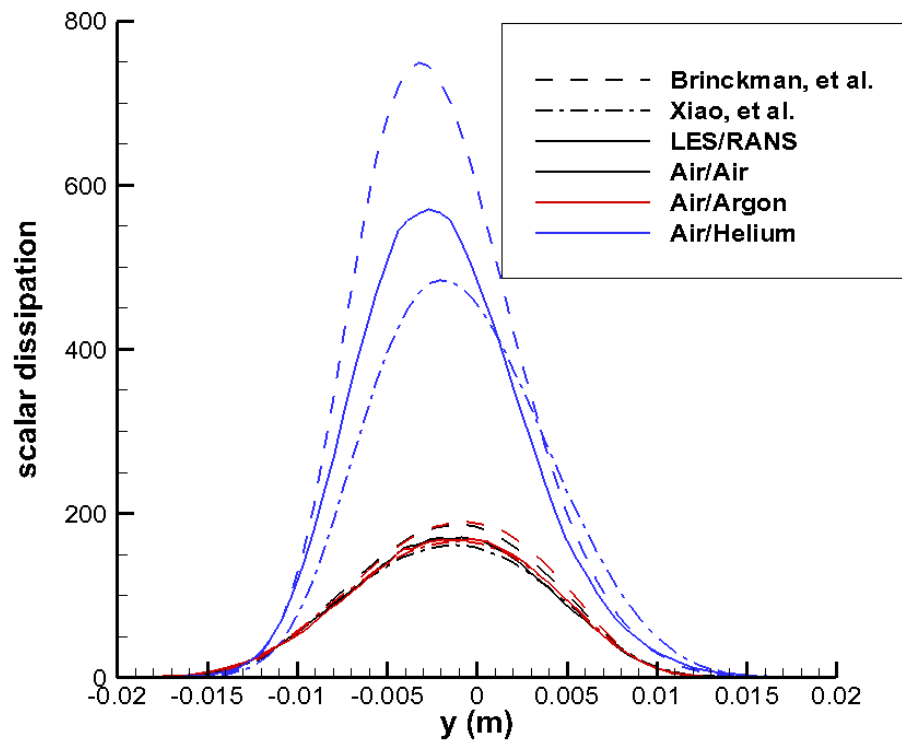


Figure 5.14: Scalar dissipation rates predicted by different models ($X = 0.25\text{m}$)

mixing case, the model consistently overpredicts the scalar variance in all regions of the flow. Figure 5.16 shows the same data taken at $x=0.25$ m from the edge of the splitter plate. The moderate overprediction of the variance for all three mixing cases is clearly visible. For the air-air and air-argon mixing cases, the models also fail to predict the increased concentration variance in the lower region of the mixing layer. The cause of this difference in profile shapes between these two cases and the helium mixing case is not immediately clear, but is probably due to the fact that the helium stream is supersonic. This suggests that the scalar turbulence can spread into the subsonic gas streams in a way that is not accounted for by the concentration variance model.

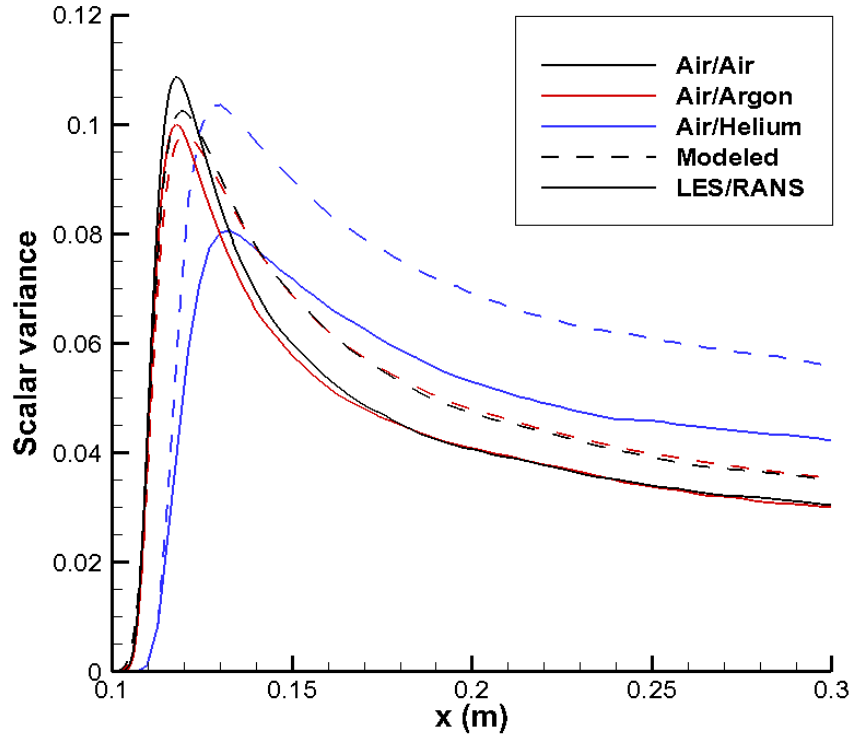


Figure 5.15: Modeled and actual concentration variance extracted along centerline of flow

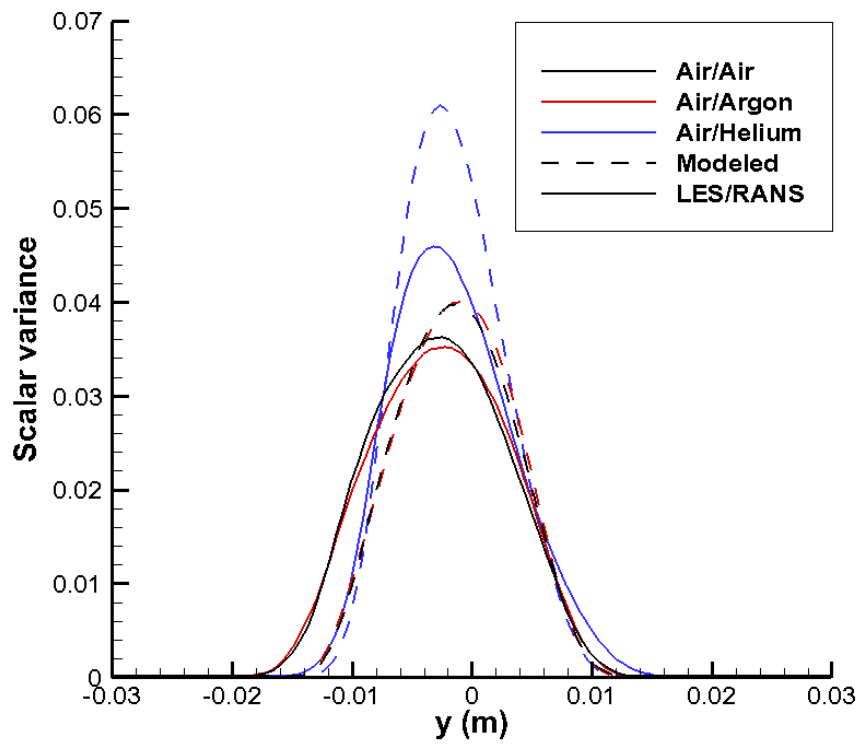


Figure 5.16: Modeled and actual concentration variance ($X = 0.25\text{m}$)

Chapter 6

LES/RANS Simulations of Sonic Injection

6.1 Calculation Details

To further assess the scalar mixing models under more complex flows, a sonic injection experiment based on Lin, et al.[15] was also simulated. Figure 6.1 outlines the layout of the experiment. A Mach 2.0 air stream moves through a rectangular test section which is 131mm high by 152mm wide. Ethylene is injected at Mach 1.0 through a 3/16" diameter circular hole, which is 5.90" downstream of the inflow, on the centerline of the test section. The computational mesh grid extends 15 injector diameters upstream of the injector, 25.5 diameters downstream, 12 diameters in the spanwise direction, and 15 in the transverse. The total mesh size is 19.96 million cells, split into 80 blocks.

This simulation had previously been carried out by Boles[4], who also utilized the REACTMB code but with a Simagorsky subgrid model and standard PPM higher-order extension for the inviscid fluxes. The numerical implementation is described in further detail in [4]. As with the planar shear layer simulation, the solution was initialized by performing a two-dimensional RANS simulation at the center plane with no injection. This solution was then extrapolated for the full domain in the spanwise direction. The starting point of the current LES/RANS simulation used in this study was the LES/RANS data obtained by Boles using the PPM scheme; the solution was progressed for a further 0.01 seconds, corresponding to approximately 25 flowthrough times. Statistics were gathered for the final 2/3 of this time. As before, in addition to the ethylene injection case presented in the experiment of Lin et. al, two more simulations were performed with argon and helium injectants. A constant momentum flux ratio of 1.5 between the injectant and air stream was maintained for all three cases. The flow conditions for the experiment are presented in Table 6.1.

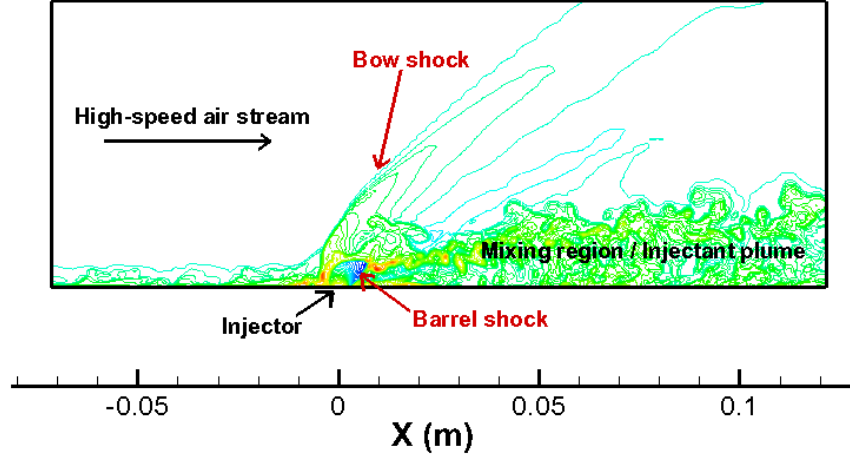


Figure 6.1: Schematic of computational domain (Lin, et. al experiment)

Table 6.1: Simulated Flow Conditions, Lin et al. Experiment

	$U_1(m/s)$	$U_2(m/s)$	$P_1(Pa)$	$P_2(Pa)$	$T_1(K)$	$T_2(K)$
Air-Ethylene	517.8	316.7	31320	219511	167.3	294.0
Air-Argon	517.8	275.8	31320	169202	167.3	250.2
Air-Helium	517.8	887.3	31320	188744	167.3	219.6

6.2 Comparison With Experiment

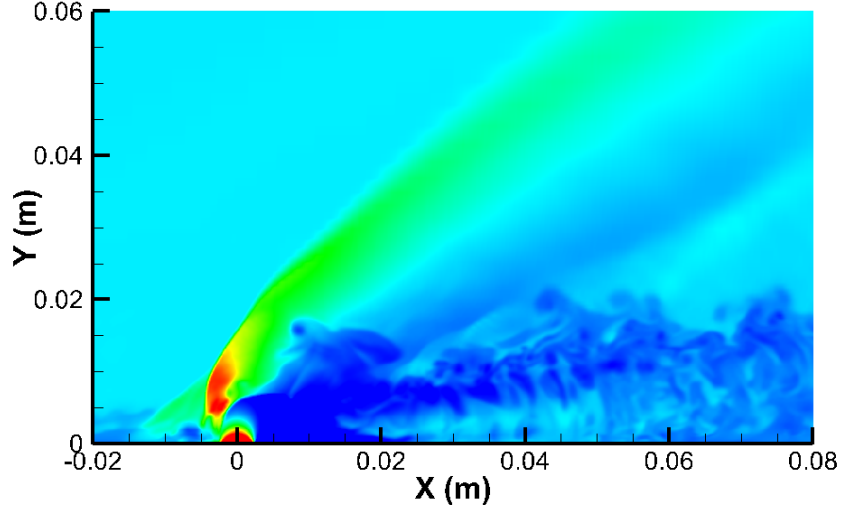


Figure 6.2: Snapshot of density contours for ethylene injection

Figure 6.2 shows a snapshot of the LES/RANS simulation taken along the centerline of the domain. The bow shock just upstream of the injector is clearly evident. The outline of the barrel shock can be seen downstream and above the injector; this is followed by a spreading, turbulent injectant plume. Validation of the LES/RANS data was accomplished by comparing the ethylene mole fraction at different y - z planes with Raman scattering and NO-PLIF data obtained by Lin, et. al. and Boles, et. al, respectively. Figure 6.3, compiled by Boles, et al shows a snapshot of the ethylene mass fraction taken at the X - Y centerline for both the simulation and the experiment. The simulation appears to be in good agreement with the experiment on first glance, although the level of jet penetration seems to be underpredicted. This can be better seen in Figure 6.4, which compares the time averaged mole fractions and standard mole fraction deviation. Figure 6.5 compares simulated ethylene mole fractions with Raman scattering data at a Y - Z plane 5 injector diameters downstream of the injector. The overall size and shape of the ethylene plume is accurately represented; however, the level of mixing is slightly underpredicted by the LES/RANS simulation and consequently the ethylene concentrations in the center of the plume are higher in the simulated data. Figure 6.6 shows the ethylene mole fraction 25 injector diameters downstream; again, the lower level of predicted mixing means an overall higher concentration of ethylene in the plume. This serves to confirm the underprediction of jet penetration and entrainment. Nevertheless, the overall structure of

the sonic injection is predicted with reasonable accuracy and we can proceed with the analysis of turbulent mixing for this case.

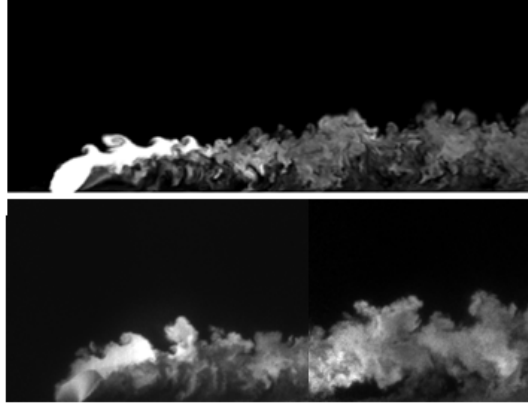


Figure 6.3: Instantaneous ethylene mass fraction predictions (top) compared with NO PLIF snapshots (bottom)

6.3 Gradient Model Evaluation

As with the shear layer simulation, turbulence statistics were gathered to assess various models for turbulent scalar mixing. Because flow created by sonic injection is much more complex than a simple shear mixing layer, the focus was first on evaluating the modeled mass diffusivity and scalar production. Figure 6.7 and Figure 6.8 show the exact and modeled scalar fluctuation production rates for ethylene injection at 5 and 25 injector diameters from the injection point, respectively. The modeled production rates in this case were calculated as $P_{S,mod} = \bar{\rho} \nu_{S,mod} \frac{\partial \tilde{Y}}{\partial x_j} \frac{\partial \tilde{Y}}{\partial x_j}$ where $\nu_{S,mod}$ were obtained from the models of Brinckman and Xiao. Additionally, the classical model utilizing a constant turbulent Schmidt number of 0.72, where $\nu_{t,mass} = \nu_{t,mom}/Sc_t$ is presented. Surprisingly, although agreement for all models is fairly good in the upstream plane, the models severely underpredict the scalar fluctuation production in the $x/d=25$ plane, where the flow is mostly developed. Furthermore, the scalar production on the underside of the plume is actually overpredicted. Further problems can be seen when looking at the modeled mass diffusivities in Figure 6.9. Here, the 'exact' diffusivity $\nu_{S,mass}$ is given by Equation 5.6. While the models underpredict the mass diffusivity in general, the actual contour shapes are radically different yet do not seem to have the expected large effect on the shape of

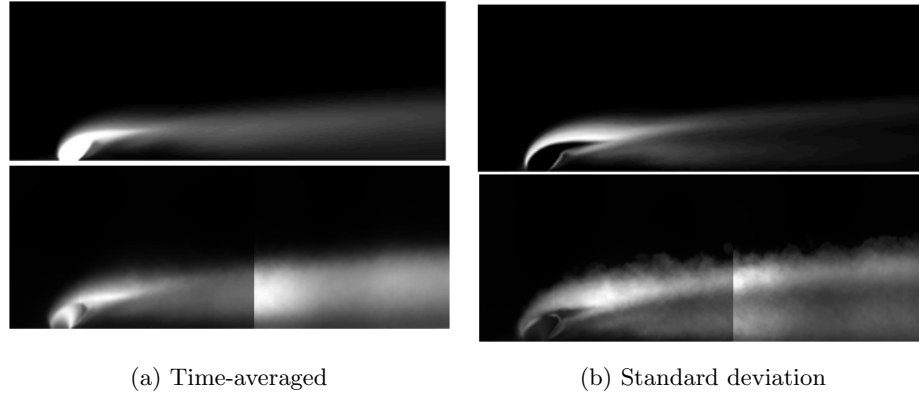


Figure 6.4: Comparison of ethylene mole fractions from simulation (top) and NO-PLIF data (bottom)

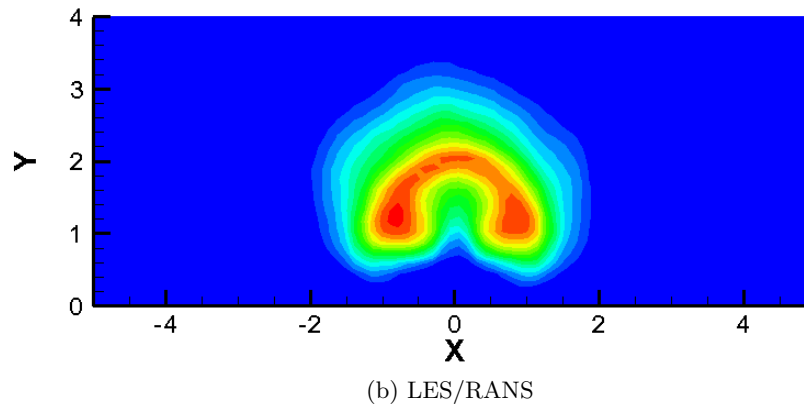
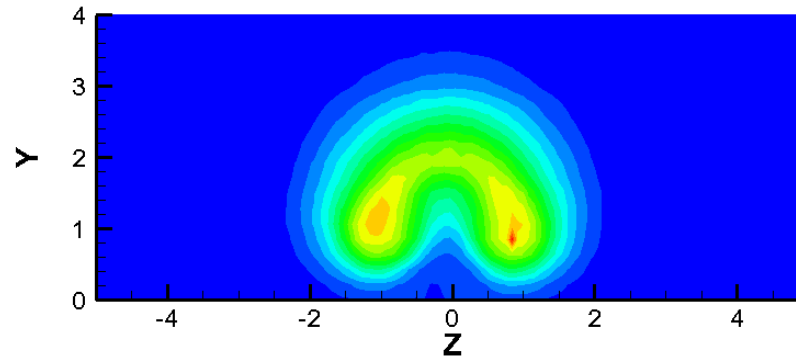
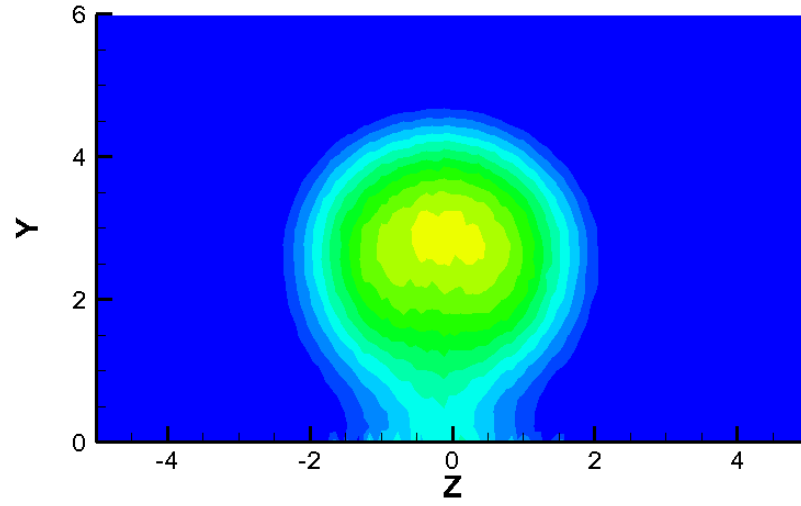
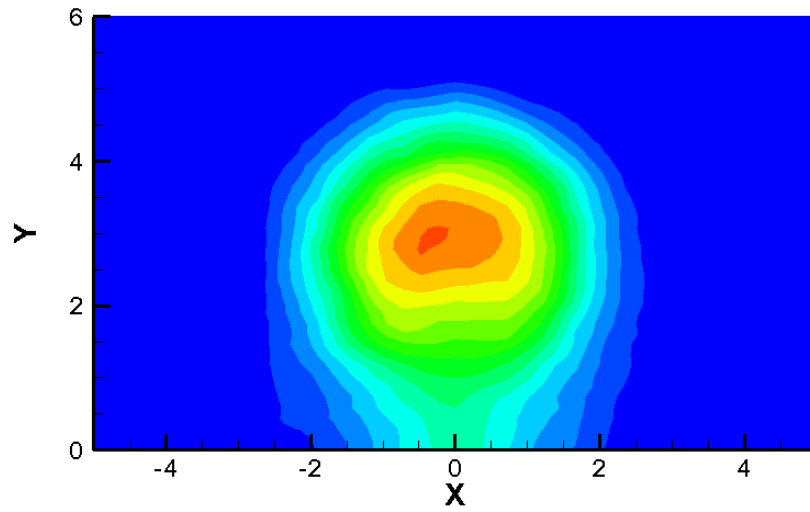


Figure 6.5: Ethylene mole fractions at $x/d = 5$. Values range from 0 to 0.7



(a) Lin, et. al



(b) LES/RANS

Figure 6.6: Ethylene mole fractions at $x/d = 25$. Values range from 0 to 0.25

the scalar production contour. It should additionally be noted that the exact mass diffusivity reaches negative values in places, which would suggest a reverse gradient-diffusion behavior for turbulent scalar flux. Clearly, we need to evaluate the basic assumptions underpinning the way scalar fluxes are modeled.

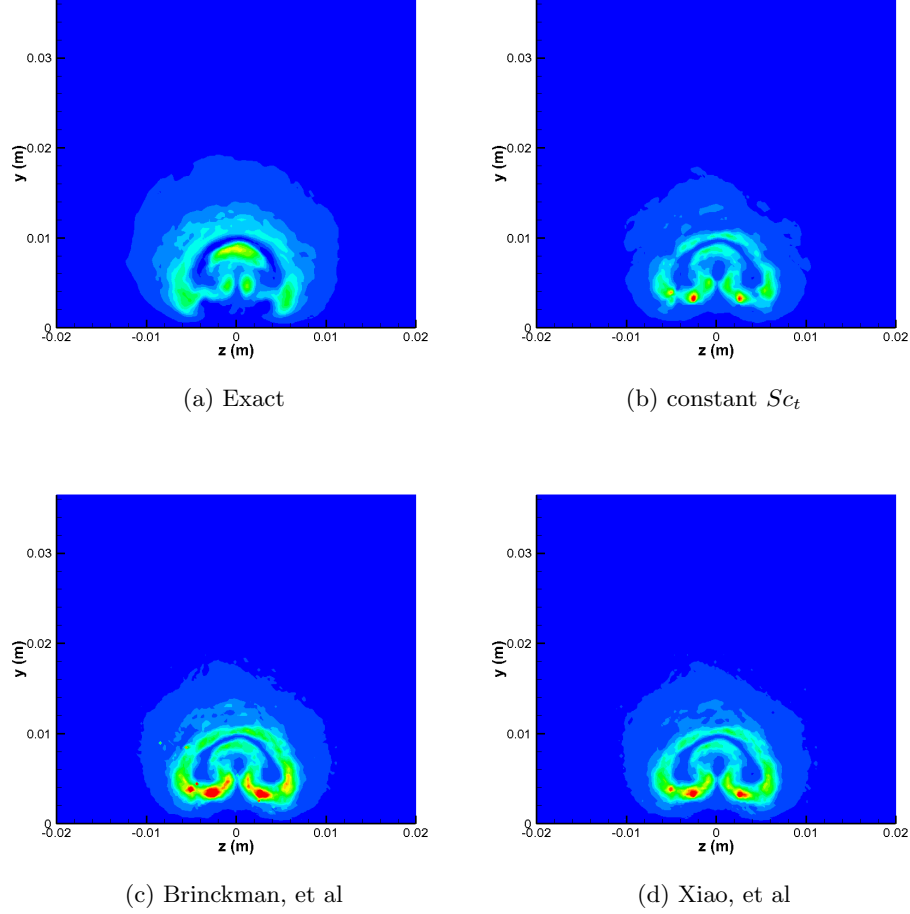
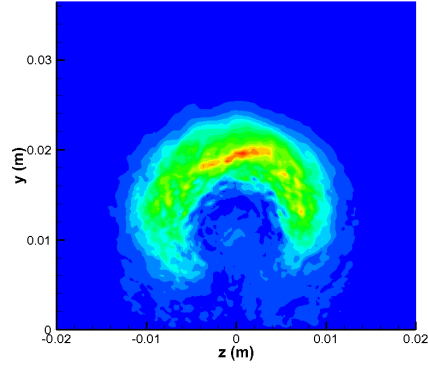


Figure 6.7: Scalar production rates for Ethylene, $x/d = 5$. Values range from 0 to $1600 \text{ kg}/\text{m}^3\text{s}$

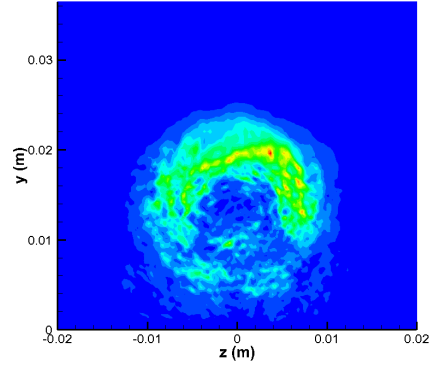
As stated previously, the turbulent scalar fluxes are classically assumed to follow a gradient diffusion model such that

$$\overline{\rho u_j'' Y''} = -\bar{\rho} \nu_{t, mass} \frac{\partial \tilde{Y}}{\partial x_j} \quad (6.1)$$

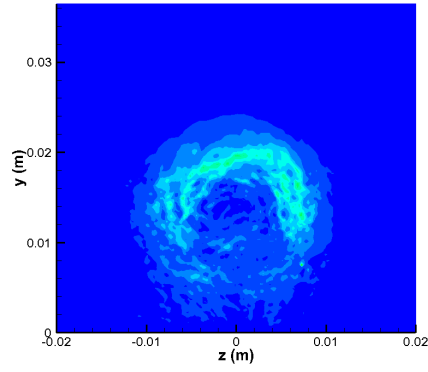
One way to test this assumption is to plot the exact fluxes from the left hand side versus the modeled fluxes on the right hand side for each point, using the 'exact' mass diffusivity as



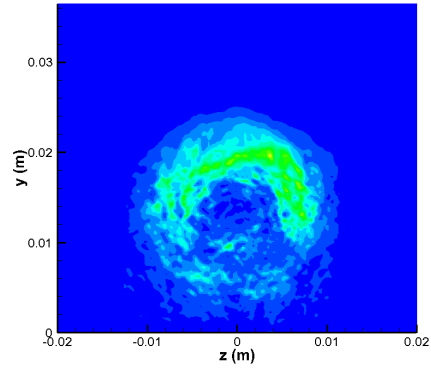
(a) Exact



(b) Contant S_{c_t}

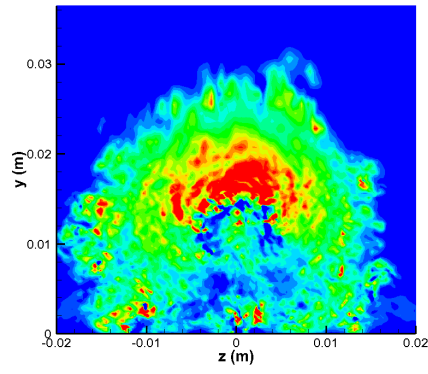


(c) Brinckman, et al

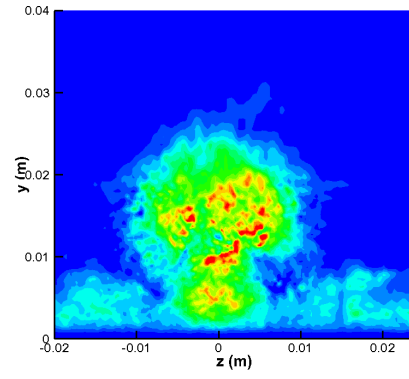


(d) Xiao, et al

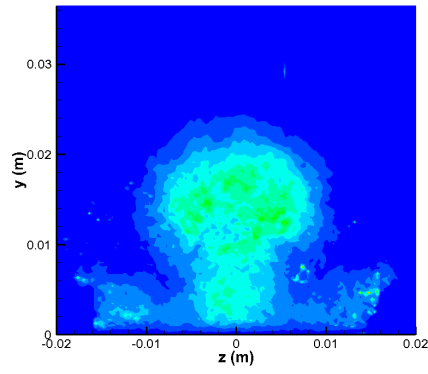
Figure 6.8: Scalar production rates for Ethylene, $x/d = 25$. Values range from 0 to $50 \text{ kg/m}^3\text{s}$



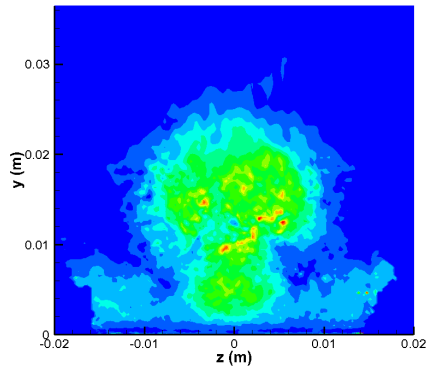
(a) Exact



(b) Constant Sc_t



(c) Brinckman, et al



(d) Xiao, et al

Figure 6.9: Mass diffusivities for Ethylene, $x/d = 25$. Values range from 0 to $0.075 \text{ m}^2/s$

determined by matching the scalar production rates (Equation 5.6). If the assumption is valid, a clear 1:1 linear relationship should be observed. Figure 6.10 shows this analysis carried out in each of the three directions for the ethylene injection flow at $x/d = 25$. It is immediately clear that while the gradient-diffusion model holds for the fluxes in the y and z directions (although with significant scatter in the y -direction), the scalar flux in the direction of flow is almost completely uncorrelated with the concentration gradients. That is, scalar fluxes in the x -direction persist even in the absence of aligned concentration gradients.

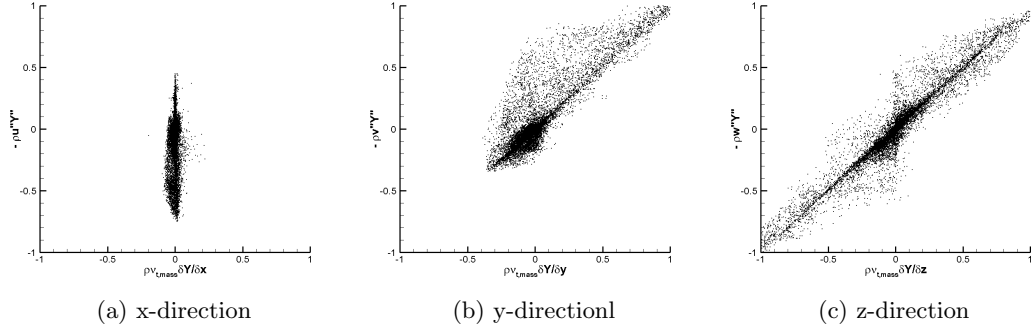


Figure 6.10: Exact versus modeled scalar fluxes for gradient-diffusion model (ethylene injection, $x/d=25$)

This problem with the gradient-diffusion model has been observed in prior research, including DNS studies of simple mixing plumes. The general consensus in the literature is that scalar fluctuation in this type of flow is generated in areas of high gradients, then transported downstream. Thus, to develop a truly accurate representation for the scalar fluxes, one would need to solve a full transport equation for each of them instead of attempting to model them based solely on local gradients.

Nevertheless, attempts have been made[26] to develop more accurate gradient models for the scalar fluxes. Younis, Speziale, and Clark developed an algebraic model based on the exact equation for the scalar flux[25],

$$\begin{aligned}
 -\overline{u'_i \theta} = & C_1 \frac{k^2}{\epsilon} \frac{\partial \Theta}{\partial x_i} + C_2 \frac{k}{\epsilon} \overline{u'_i u'_j} \frac{\partial \Theta}{\partial x_j} \\
 & + C_3 \frac{k^3}{\epsilon^2} \frac{\partial U_i}{\partial x_j} \frac{\partial \Theta}{\partial x_j} + C_4 \frac{k^2}{\epsilon^2} \left(\overline{u'_i u'_k} \frac{\partial U_j}{\partial x_k} + \overline{u'_j u'_k} \frac{\partial U_i}{\partial x_k} \right) \frac{\partial \Theta}{\partial x_j}
 \end{aligned} \tag{6.2}$$

where Θ represents a generic scalar, k is the turbulent kinetic energy, and ϵ is the turbulent

dissipation. The scalar fluxes in this formulation depend not only on the parallel concentration gradients, but on the normal gradients, velocity gradients, and turbulent momentum terms. While this model does not include a characteristic viscosity term, we note that the term k^2/ϵ has the same units as ν_t . Hence, the model can be adapted to fit into our previous framework by equating these two quantities. Ignoring the last two terms and accounting for density fluctuation, the adjusted model for the scalar flux can be written:

$$-\overline{\rho u_i'' Y''} = \bar{\rho} \nu_{t, mass} \left(C_1 \frac{\partial \tilde{Y}}{\partial x_i} + C_2 \frac{\overline{\rho u_i'' u_j''}}{\bar{\rho} k} \frac{\partial \tilde{Y}}{\partial x_j} \right) \quad (6.3)$$

The key difference between this new model and the standard linear gradient formulation is the dependence of the scalar fluxes on normal gradients, which provides the ability to predict scalar transport in one direction even in the absence of co-directional concentration gradients. Additionally, the model partially accounts for convection mixing due to turbulence by including a dependence on the turbulent momentum flux. The ratio of the constants C_1 and C_2 is determined by plotting the exact and predicted scalar fluxes as in Figure 6.10 and adjusting the constants until a linear fit has a slope of 1. Both constants are then scaled by matching the exact scalar production rate $-\overline{\rho u_i'' Y''} \frac{\partial \tilde{Y}}{\partial x_i}$ with the modeled form,

$$\bar{\rho} \nu_{t, mass} \left(C_1 \frac{\partial \tilde{Y}}{\partial x_i} + C_2 \frac{\overline{\rho u_i'' u_j''}}{\bar{\rho} k} \frac{\partial \tilde{Y}}{\partial x_j} \right) \frac{\partial \tilde{Y}}{\partial x_i} \quad (6.4)$$

for ethylene injection at three different planes. The final constants used in this study are $C_1 = -0.5$ and $C_2 = 1.6$. A comparison of the exact and modeled scalar fluxes in each direction is shown in Figure 6.11. The new model maintains a linear correlation in the y- and z-direction fluxes while also introducing a correlation in the x-direction fluxes, although the linear fit is far from perfect. Given the improvement over a classical gradient-diffusion model, the new formulation is adopted for the rest of this study.

Figures 6.12-6.20 show the exact and modeled scalar production rates for all three gas mixing cases and profiles. The modeled production rates use the new constitutive relation for the scalar fluxes, along with mass diffusivities taken from the models of Brinckman, Xiao, and the constant turbulent Schmidt number assumption. From these we can draw some general conclusions about the performance of the models. For ethylene injection, we can immediately see that the overprediction of scalar production at the bottom of the plume is significantly lessened, and the overall contour shapes for all models match the exact production fairly closely. The models agree with the exact production rate very closely at the $x/d=15$ plane. However, as we move into the far-field, the models underpredict the overall scalar production rate quite significantly; this is especially true when using the mass diffusivity of Brinckman, et al. This

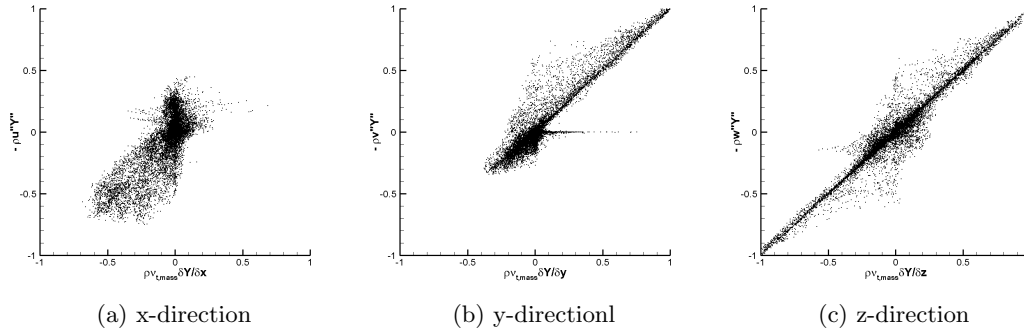


Figure 6.11: Exact versus modeled scalar fluxes for new model ethylene injection, $x/d = 25$)

can be largely explained by a general under-prediction of the mass diffusivity by all models, which was apparent from Figure 6.9. A similar pattern is seen for the other two gas injection cases. The scalar production is fairly well predicted in the $x/d=5$ and $x/d=15$ planes, but is underpredicted in the $x/d=25$ plane. For helium injection, the underprediction becomes apparent even further upstream. However, the proportional distribution of scalar production is matched very well for all cases, which suggests that better predictions can be obtained solely through different scaling. This could be accomplished either with altering the model constants used in the constitutive relation for the scalar fluxes, or by adjusting the mass diffusivity models of Brinckman and Xiao. One potential fix for the latter would be to include the momentum eddy viscosity in the definition of the mass diffusivity, as was done when designing the 'optimized' mass diffusivity models in the planar shear layer simulation. However, this has not been carried out in the current study. It must be noted that the assumption of a constant turbulent Schmidt number provides an estimate of the scalar production that is in most cases equal to or better than that of either of the two flow-based models. In particular, the underestimation of scalar production in the far-field is noticeably lessened in all three flow cases. It appears that if an approximate value of the turbulent Schmidt number is known *a priori*, there is no disadvantage to using this much simpler mass diffusivity model in a RANS-level solution. However, as noted earlier, a good estimate of the Schmidt number is not always known when doing a predictive study, and the models of Brinckman and Xiao can offer similarly valid predictions of the scalar flux without the need to specify any extra parameters.

6.4 Effect of Convergence

One issue which could impact model performance for this simulation is the overall convergence of the flow solution. It is possible that errant unsteady concentration gradients would cause

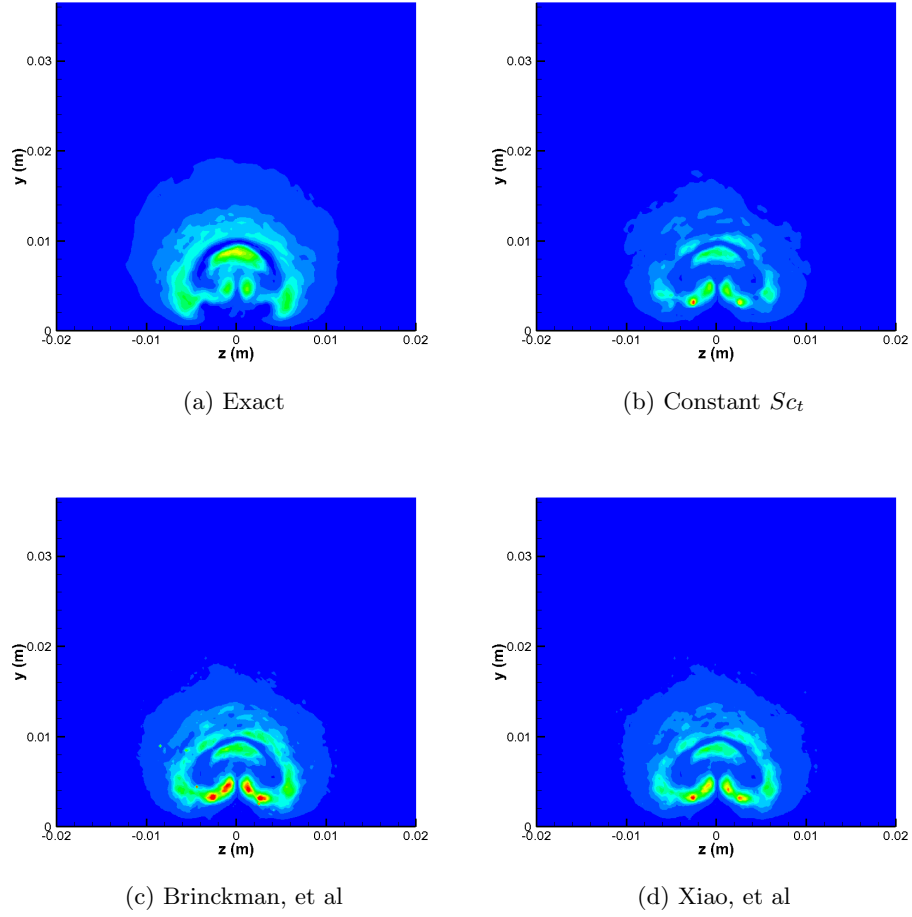
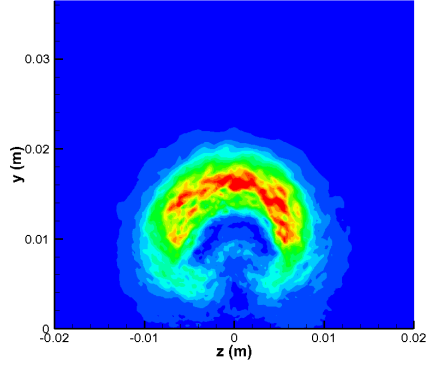
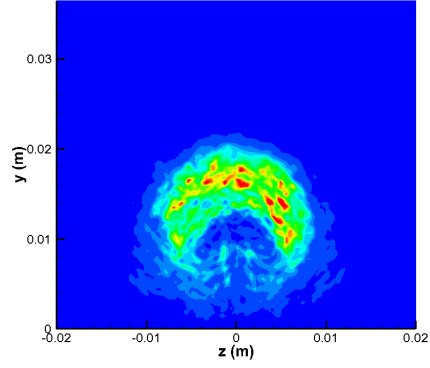


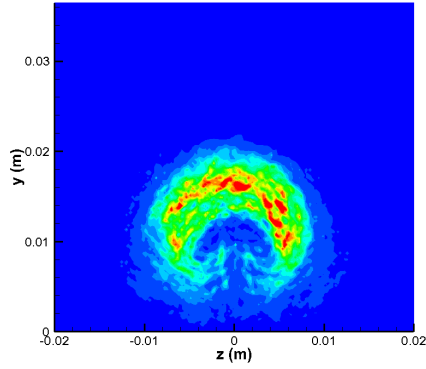
Figure 6.12: Scalar production rates for Ethylene, $x/d = 5$. Values range from 0 to 1600 kg/m^3s



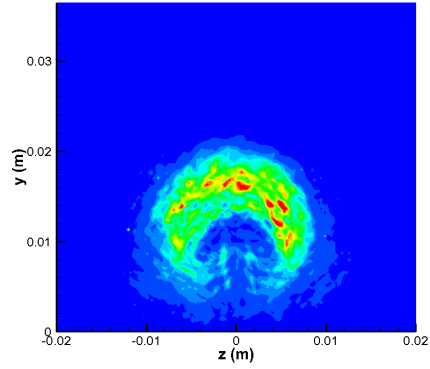
(a) Exact



(b) Constant Sc_t

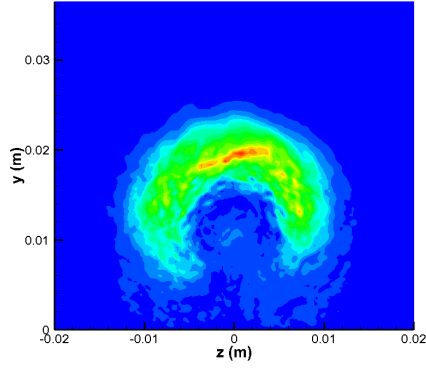


(c) Brinckman, et al

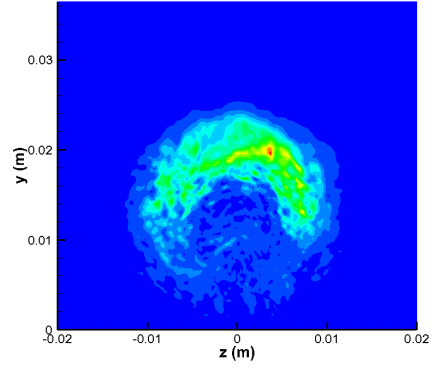


(d) Xiao, et al

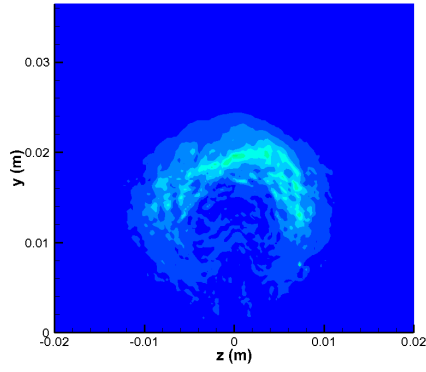
Figure 6.13: Scalar production rates for Ethylene, $x/d = 15$. Values range from 0 to 100 kg/m^3s



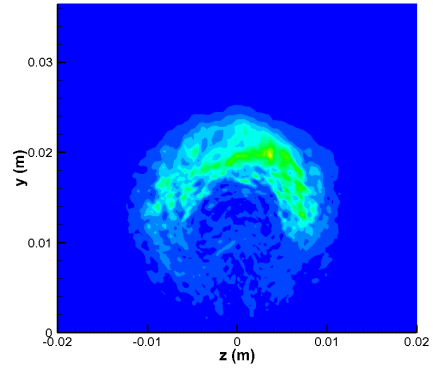
(a) Exact



(b) Constant Sc_t

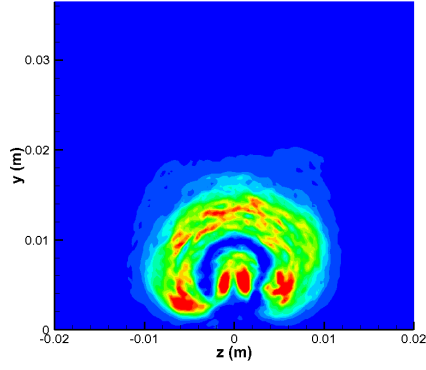


(c) Brinckman, et al

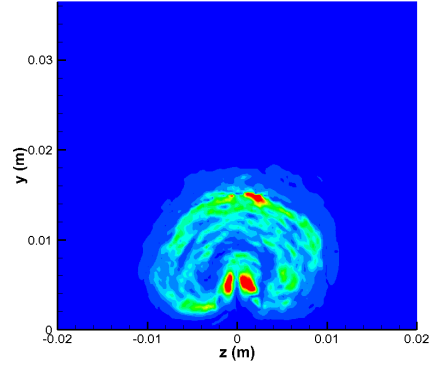


(d) Xiao, et al

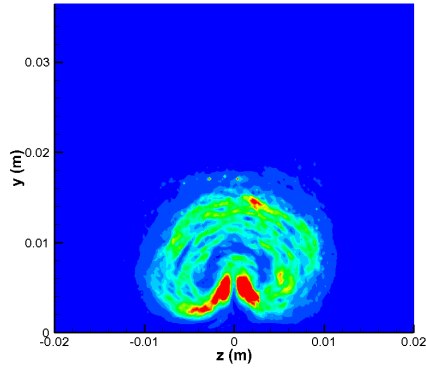
Figure 6.14: Scalar production rates for Ethylene, $x/d = 25$. Values range from 0 to $50 \text{ kg/m}^3\text{s}$



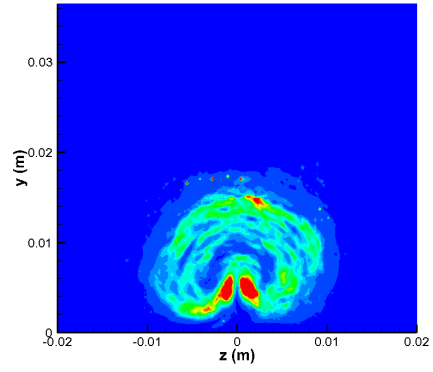
(a) Exact



(b) Constant Sc_t

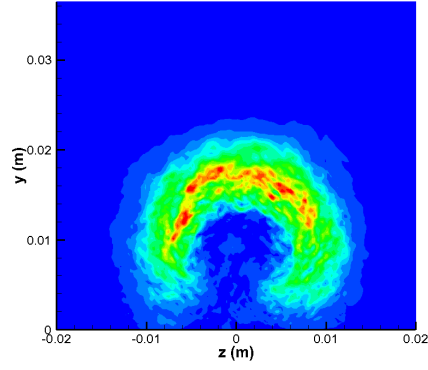


(c) Brinckman, et al

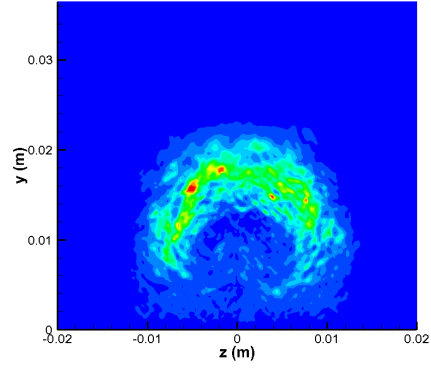


(d) Xiao, et al

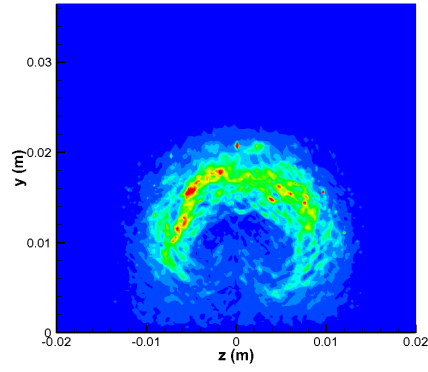
Figure 6.15: Scalar production rates for Argon, $x/d = 5$. Values range from 0 to $600 \text{ kg/m}^3\text{s}$



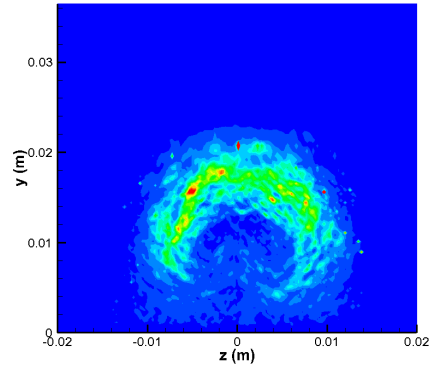
(a) Exact



(b) Constant Sc_t

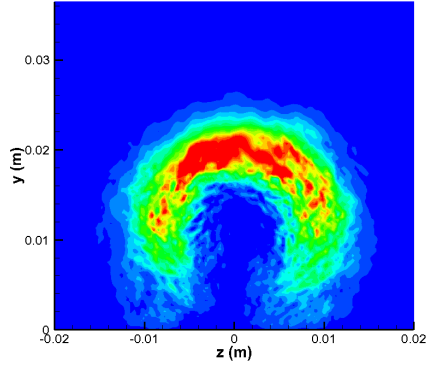


(c) Brinckman, et al

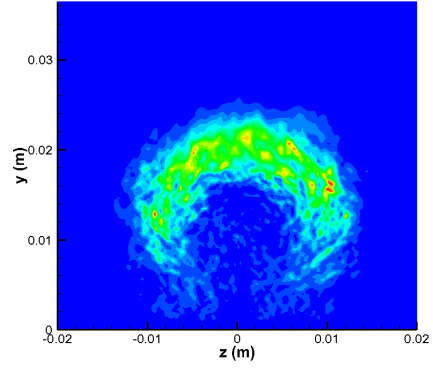


(d) Xiao, et al

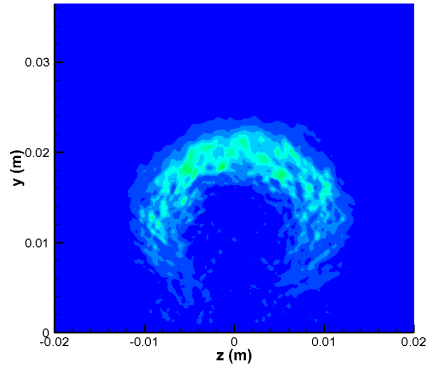
Figure 6.16: Scalar production rates for Argon, $x/d = 15$. Values range from 0 to $80 \text{ kg/m}^3\text{s}$



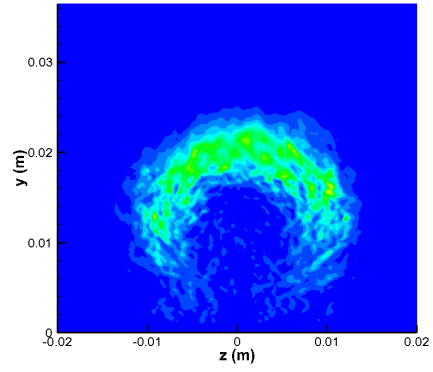
(a) Exact



(b) Constant Sc_t

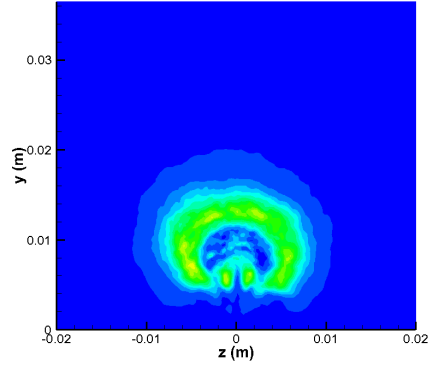


(c) Brinckman, et al

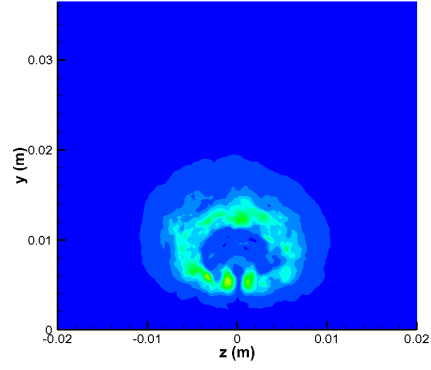


(d) Xiao, et al

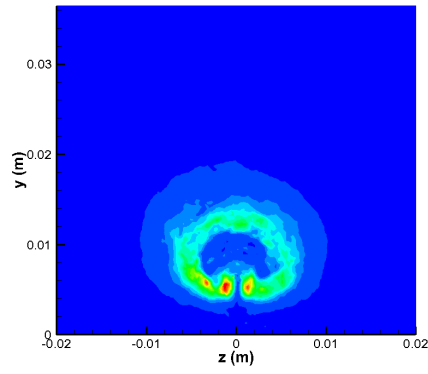
Figure 6.17: Scalar production rates for Argon, $x/d = 25$. Values range from 0 to $25 \text{ kg/m}^3\text{s}$



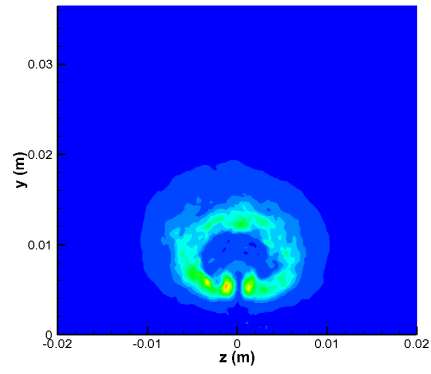
(a) Exact



(b) Constant Sc_t

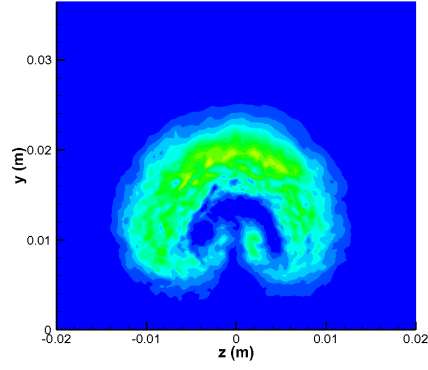


(c) Brinckman, et al

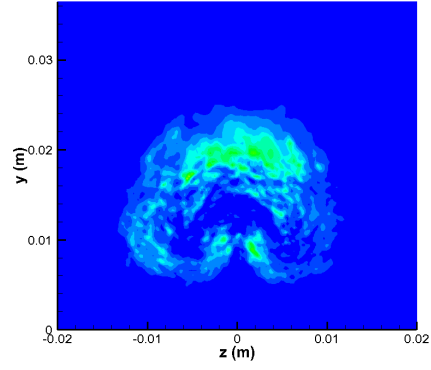


(d) Xiao, et al

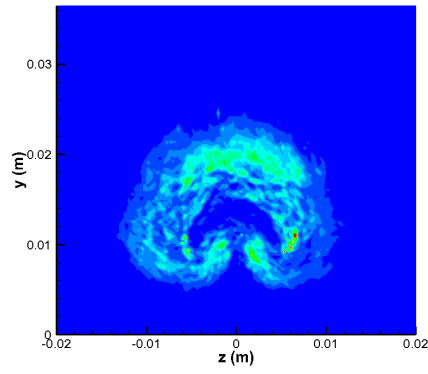
Figure 6.18: Scalar production rates for Helium, $x/d = 5$. Values range from 0 to $300 \text{ kg/m}^3\text{s}$



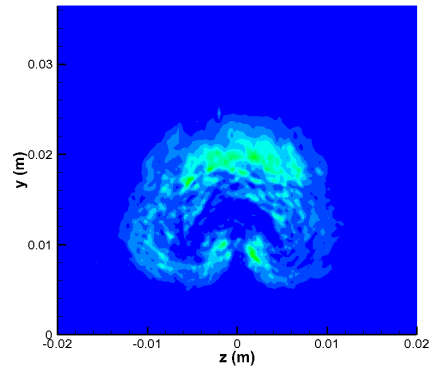
(a) Exact



(b) constant Sc_t

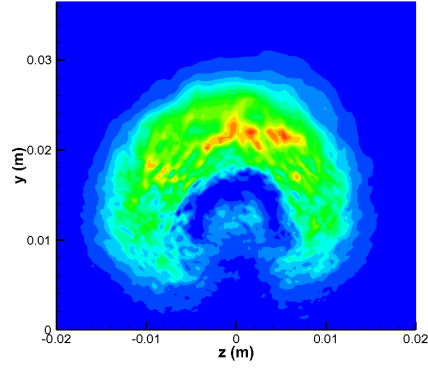


(c) Brinckman, et al

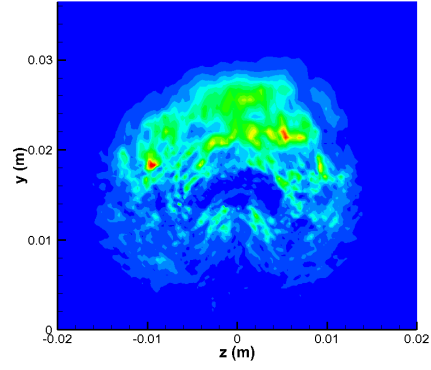


(d) Xiao, et al

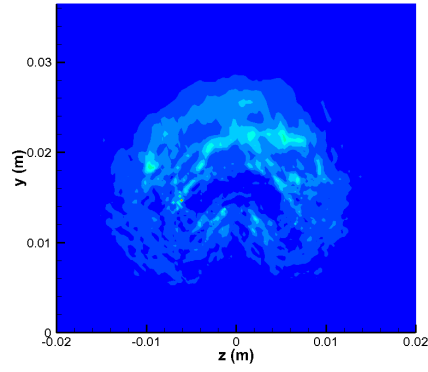
Figure 6.19: Scalar production rates for Helium, $x/d = 15$. Values range from 0 to $15 \text{ kg/m}^3\text{s}$



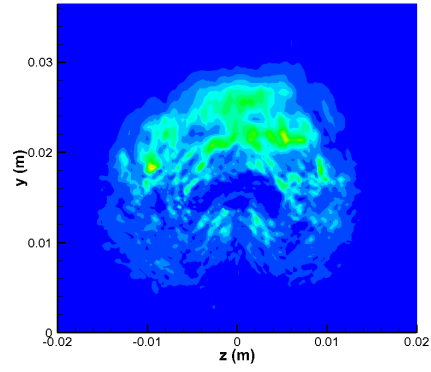
(a) Exact



(b) Constant Sc_t



(c) Brinckman, et al



(d) Xiao, et al

Figure 6.20: Scalar production rates for Helium, $x/d = 25$. Values range from 0 to $3 \text{ kg/m}^3\text{s}$

either the mass diffusivity models or the gradient-diffusion model to break down. This was tested by running a second simulation of argon injection for an additional 0.01s (approximately 20 flowthrough times) and collecting additional time-averaged statistics over that time period, ensuring a smoother solution. The results were compared with the 'unconverged' simulation for the same configuration, which was run for half of that time. (Figure 6.21) The top row in the figure displays the exact and modeled scalar production rates for the extra converged simulation; in the case, the modeled scalar production rates assume the classic gradient-diffusion model for the scalar fluxes. Although it is clear that the extra convergence reduces some of the noise and fluctuations in the scalar production data, the overall contour shapes and magnitudes are unchanged for both the exact and modeled data. It is clear from this that the performance issues of the scalar flux models are due to structural deficiencies in the models themselves, rather than the degree of smoothness of the flow data.

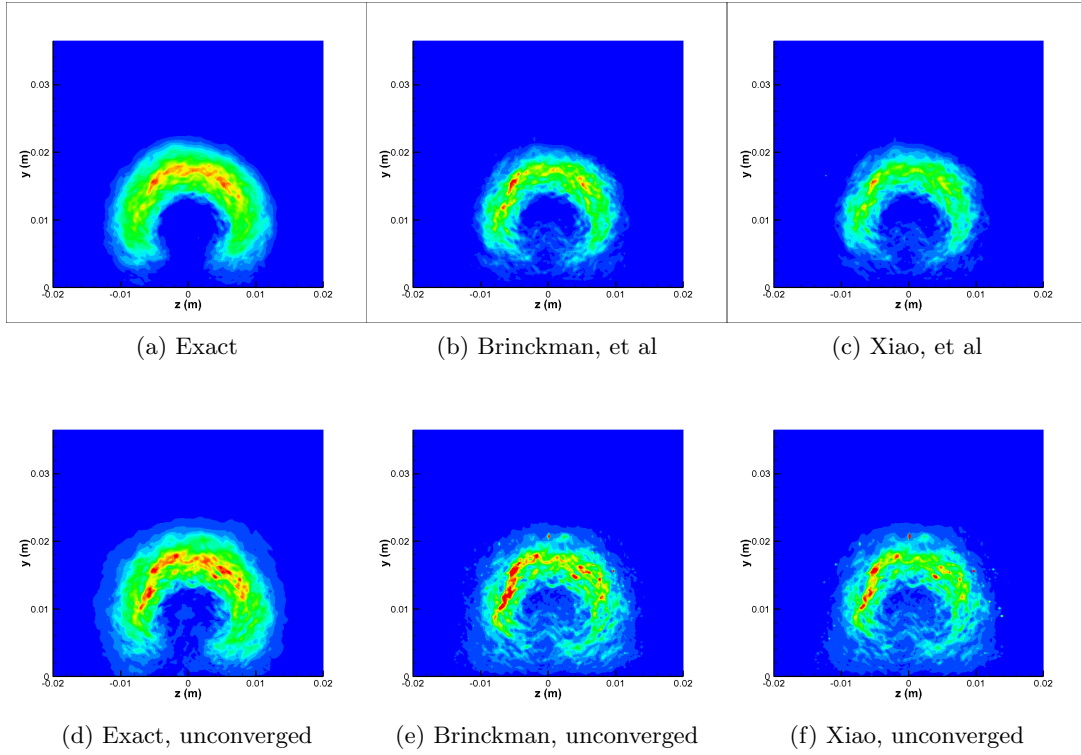


Figure 6.21: Scalar production rates for Argon, $x/d = 15$. Values range from 0 to $80 \text{ kg/m}^3\text{s}$

Chapter 7

Summary and Conclusions

In this study, a hybrid LES/RANS method was used to simulate two different types of supersonic gas mixing experiments. The solver uses large eddy simulation (LES) with a Lenormand subgrid model away from the walls and a Reynolds-averaged Navier Stokes method with a Menter BSL turbulence closure near the walls. Large-scale turbulence is introduced and sustained via a recycling-rescaling technique at the inflow. Flux calculations are extended to higher order accuracy by a Low-dissipation Piecewise Parabolic Method which uses a vorticity-dependent blending function to preserve monotonicity only in shock-dominated regions.

A planar mixing layer simulation based on the experiment of Barre, et al was performed. Streams of air, argon, and helium were mixed in parallel with a Mach 1.3 air stream. Comparisons with experimental data in the air-air mixing case yielded good agreement for the gas velocities, velocity fluctuation, and temperature fluctuations. The shear layer spreading rate was found to be higher than indicated in the experimental data, although it was in good agreement with other data in the literature.

A sonic injection experiment by Lin, et al. was also simulated, with ethylene, argon, and helium injected from a 3/16" diameter circular opening into a Mach 2.0 air crossflow. Ethylene mole fraction data obtained from the simulation was compared with Raman scattering and NO PLIF data from the experiment, where it was found that the jet penetration and entrainment were slightly underpredicted in the numerical study.

Turbulence statistics were gathered from all of the numerical experiments and used to evaluate two RANS-level models for turbulent scalar transport by Brinckman, et al and Xiao, et al. The model of Xiao, et al was successful at predicting the mass transport eddy viscosity for all three planar mixing flows. The scalar fluctuation production rate for the same experiment was predicted with very good accuracy by both models after some rescaling, although the model of Brinckman, et al had to be adjusted to include the momentum eddy viscosity in its formulation of the mass eddy viscosity. Analysis of some modeled constituent terms yielded mixed results.

Both the mass fraction variance and scalar dissipation rate were predicted well in the far-field by the model of Xiao, and were slightly overpredicted by that of Brinckman. However, both models failed in the near-field, where higher gradients and levels of turbulence were present.

The models were far less successful for the sonic injection case. It was found that the classical gradient-diffusion formulation for the scalar fluxes failed to predict a turbulent flux in the direction of the flow in the absence of concentration gradients. A new model based on the work of Younis, et al, which includes a dependence on the normal concentration gradients and turbulent kinetic energy, was proposed. This new formulation was found to correlate better with the exact scalar fluxes in all directions. Employing the two mass diffusivity models in this framework yielded decent prediction of scalar production rates in the near field of all three gas mixing cases. However, both of the models significantly underpredicted the scalar production rates in the far-field in every case, likely due to the very low concentration gradients in those regions. Additionally, neither model offered a clear advantage over simply assuming a constant turbulent Schmidt number.

Better model performance could be obtained for the sonic injection simulations if both mass diffusivity models were re-scaled and adjusted to include turbulent momentum terms. Of course, literature suggests that any turbulent scalar flux models based only on local gradients will have limited accuracy in complex flows, since the fluctuations themselves are transported from farther upstream. Still, modeling the scalar fluxes in this fashion hold promise for conducting predictive RANS simulations of gas mixing. It remains to evaluate the modeled constituent terms (mass fraction variance and scalar dissipation) for the sonic injection case. The new non-classical gradient diffusion formulation must be tested for the planar shear layer. Finally, before either model can be implemented, they must be tested in an actual RANS simulation using full modeling of constituent terms.

REFERENCES

- [1] S. Barre, C. Quine, and J.P. Dussauge. Compressibility effects on the structure of supersonic mixing layer: experimental results. *Journal of Fluid Mechanics*, 259, 1994.
- [2] R. A. Baurle and D.R. Eklund. Analysis of dual mode hydrocarbon scramjet operation at Mach 4-6.5. *Journal of Propulsion and Power*, 18(5):990–1002, 2002.
- [3] P.S. Bernard and A.L. Rovelstad. On the physical accuracy of scalar transport modeling in inhomogeneous turbulence. *Physics of Fluids*, 6(9):3093–3108, 1994.
- [4] J.A. Boles. *Hybrid Large-Eddy Simulation/Reynolds-Averaged Navier-Stokes Methods and Predictions for Various High-Speed Flows*. PhD thesis, North Carolina State University, 2009.
- [5] J.A. Boles, J-I. Choi, J.R. Edwards, and R.A. Baurle. simulations of high-speed internal flows using LES/RANS models. 2009. AIAA Paper 2009-1324.
- [6] K. Brinckman, W.H. Calhoon, and S.M. Dash. Scalar fluctuation modeling for high-speed aeropropulsive flows. *AIAA Journal*, 45(5):1036 – 1046, 2007.
- [7] P. Colella and P.R. Woodward. The piecewise parabolic method (PPM) for gas-dynamical simulations. *Journal of Computational Physics*, 54:174–201, 1984.
- [8] F. Ducros, V. Ferrand, F. Nicaud, C. Weber, D. Darracq, C. Gachareiu, and T. Poinso. Large-eddy simulation of the shock / turbulence interaction. *Journal of Computational Physics*, 152(2):517–549, 1999.
- [9] J.R. Edwards, J-I. Choi, and J.A. Boles. Hybrid large-eddy / reynolds-averaged Navier-Stokes simulation of a mach-5 compression corner interaction. *AIAA Journal*, 46(4):977–991, 2008.
- [10] A Low-Diffusion Flux-Splitting Scheme for Navier-Stokes Calculations. *Computers and Fluids*, 26(6):635–659, 1997.
- [11] D.A. Giesecking, J-I. Choi, J.R. Edwards, and H.A. Hassan. Compressible flow simulations using a new LES/RANS model. *AIAA Journal*, 2012. To appear.
- [12] P.G. Keistler. *A variable turbulent Prandtl and Schmidt number model for scramjet application*. PhD thesis, North Carolina State University, 2008.
- [13] P.G. Kiestler and H.A. Hassan. Simulation of supersonic combustion involving H_2 /air and C_2H_4 /air. January 2009. AIAA Paper 2009-29.
- [14] E. Lenormand, P. Sagaut, L. Ta Phuoc, and P. Compte. Subgrid-scale models for large-eddy simulations of compressible, wall-bounded flows. *AIAA Journal*, 38:1340–1350, 2000.
- [15] K. Lin, M. Ryan, C. Carter, M. Gruber, and C. Raffoul. Scalability of ethylene gaseous jets for fueling high-speed air-breathing combustors. In *47th Aerospace sciences meeting*, Orlando, USA, 2009. AIAA Paper 2009-1423.

- [16] B. J. McBride, S. Gordon, and M.A Reno. Coefficients for calculating thermodynamic and transport properties of individual species. Technical report, NASA.
- [17] F.R. Menter. Two-equation eddy-viscosity turbulence models for engineering applications. *AIAA Journal*, 32(8):1598–1605, August 1994.
- [18] D.F. Robinson and H.A. Hassan. further developmets in the $k-\zeta$ (enstrophy) turbulence closure model. *AIAA Journal*, 36(10):1825–1883, 1998.
- [19] T.P. Sommer, R.M.C. So, and H.S. Zhang. Near-wall variable prandtl number turbulence model for compressible flows. *AIAA Journal*, 31(1):22–35, 1993.
- [20] J. Tomes, C. Kannepalli, W.H. calhoon, and J.M. Seiner. Studies to validate scalar fluctuation modeling in high speed jet interaction flowfields. January 2009. AIAA Paper 2009-1115.
- [21] R.J. Ungewitter, K. Brinckman, and S.M. Dash. Advanced modeling of new fuel/air mixing data sets for scramjet applications. August 2009. AIAA Paper 2009-4940.
- [22] M.A. Vyas, W.A. Engblom, N.J. Georgiadis, C.J. Trefney, and V.A. Bhagwandin. Numerical simulation of vitiation effects on a hydrogen-fueled dual-mode scramjet. January 2010. AIAA Paper 2010-1127.
- [23] David C. Wilcox. *Turbulence Modeling for CFD, Second Edition*. DCW Industries, 1998.
- [24] X. Xiao, J.R. Edwards, H.A. Hassan, and A.D. Cutler. Variable Schmidt number formulation for scramjet applications. *AIAA Journal*, 44(3):593–599, 2006.
- [25] B.A. Younis, C.G. Speziale, and T. T. Clark. A rational model for the turbulent scalar fluxes. *Proceedings of the Royal society*, 461:575–594, 2005.
- [26] Bassam A Younis. Progress in modeling scalar transport in 'complex' turbulent shear flows. *Mecanica Computacional*, 23, 2004.